



**HAL**  
open science

## **TopBP1 assembles nuclear condensates to switch on ATR signalling**

Camilla Frattini, Alexy Promonet, Emile Alghoul, Sophie Vidal-Eychenie, Marie Lamarque, Marie-Pierre Blanchard, Serge Urbach, Jihane Basbous, Angelos Constantinou

► **To cite this version:**

Camilla Frattini, Alexy Promonet, Emile Alghoul, Sophie Vidal-Eychenie, Marie Lamarque, et al.. TopBP1 assembles nuclear condensates to switch on ATR signalling. *Molecular Cell*, 2021, 81 (6), pp.1231-1245.e8. 10.1016/j.molcel.2020.12.049 . inserm-03252517

**HAL Id: inserm-03252517**

**<https://inserm.hal.science/inserm-03252517>**

Submitted on 7 Jun 2021

**HAL** is a multi-disciplinary open access archive for the deposit and dissemination of scientific research documents, whether they are published or not. The documents may come from teaching and research institutions in France or abroad, or from public or private research centers.

L'archive ouverte pluridisciplinaire **HAL**, est destinée au dépôt et à la diffusion de documents scientifiques de niveau recherche, publiés ou non, émanant des établissements d'enseignement et de recherche français ou étrangers, des laboratoires publics ou privés.

1 **TopBP1 assembles nuclear condensates to switch on ATR signalling.**

2 Camilla FRATTINI<sup>1</sup>, Alexy PROMONET<sup>1</sup>, Emile ALGHOUL<sup>1</sup>, Sophie VIDAL-EYCHENIE<sup>1</sup>,  
3 Marie LAMARQUE<sup>1</sup>, Marie-Pierre BLANCHARD<sup>1</sup>, Serge URBACH<sup>2</sup>, Jihane BASBOUS<sup>1,4</sup> and  
4 Angelos CONSTANTINO<sup>1,3,4</sup>

5

6

7

8

9 1 Institut de Génétique Humaine - CNRS - Université de Montpellier

10 2 Institut de Génomique Fonctionnelle - CNRS INSERM - Université de Montpellier

11 3 Lead contact

12 4 Correspondance : [jihane.basbous@igh.cnrs.fr](mailto:jihane.basbous@igh.cnrs.fr); [angelos.constantinou@igh.cnrs.fr](mailto:angelos.constantinou@igh.cnrs.fr)

13

14 **Summary**

15

16 **ATR checkpoint signalling is crucial for cellular responses to DNA replication impediments.**

17 **Using an optogenetic platform, we show that TopBP1, the main activator of ATR, self-**

18 **assembles extensively to yield micron-sized condensates. These opto-TopBP1 condensates**

19 **are functional entities organized in tightly packed clusters of spherical nano-particles.**

20 **TopBP1 condensates are reversible, occasionally fuse and co-localise with TopBP1 partner**

21 **proteins. We provide evidence that TopBP1 condensation is a molecular switch that amplifies**

22 **ATR activity to phosphorylate checkpoint kinase 1 (Chk1) and slowdown replication forks.**

23 **Single amino acid substitutions of key residues in the intrinsically disordered ATR-activation**

24 **domain disrupt TopBP1 condensation and, consequently, ATR/Chk1 signalling. In**

25 **physiologic salt concentration and pH, purified TopBP1 undergoes liquid-liquid phase**

26 **separation *in vitro*. We propose that the actuation mechanism of ATR signalling is the**

27 **assembly of TopBP1 condensates driven by highly regulated multivalent and cooperative**

28 **interactions.**

## 29 **Introduction**

30 The primary structure of DNA is subjected to constant chemical alterations caused by spontaneous  
31 decay, endogenous metabolites and environmental genotoxic agents (Friedberg et al., 2006;  
32 Lindahl, 1993), hence organisms have evolved multiple DNA repair mechanisms to ensure  
33 genome integrity and survival (Ciccia and Elledge, 2010; Jackson and Bartek, 2009; Tubbs and  
34 Nussenzweig, 2017). DNA damage sensors, protein scaffolds and DNA processing activities  
35 accumulate at DNA damage sites to form spatially defined and reversible structures commonly  
36 referred to as nuclear foci (Garcia-Higuera et al., 2001; Lisby et al., 2001; Maser et al., 1997; Park  
37 et al., 1996). Much still remains to be understood about the molecular forces that drive the  
38 formation of DNA damage foci and their functional consequences in the DNA damage response.

39 In recent years, application of the principles of polymer chemistry to biological molecules  
40 has accelerated spectacularly our understanding of the assembly mechanism and functions of  
41 membraneless compartments (Banani et al., 2017; Bracha et al., 2019; Hyman and Simons, 2012;  
42 Shin and Brangwynne, 2017; Soding et al., 2020). These self-organized micron-scale structures,  
43 called biomolecular condensates, assemble via multiple weak, cooperative and dynamic  
44 interactions and yield a rich repertoire of higher-order structures with diverse physical properties,  
45 variable size, and no defined stoichiometry of constituent proteins. Whereas nucleic acids can  
46 serve a seeding platform for the self-organization of soluble proteins (Mao et al., 2011;  
47 McSwiggen et al., 2019), soluble bridging factors can cross-link chromatin segments to  
48 compartmentalize chromatin via a process of polymer-polymer phase separation (Erdel et al.,  
49 2020). Increasing evidence indicates that diverse multivalent protein scaffolds self-organize via  
50 liquid-liquid phase separation, a process of de-mixing that yields a condensed phase enriched in  
51 the protein and a dilute phase (Banani et al., 2017; Shin and Brangwynne, 2017). Biomolecular

52 condensates are functional hubs implicated in diverse cellular processes, including innate immune  
53 signalling (Du and Chen, 2018), microtubule nucleation (Woodruff et al., 2017), transcription  
54 (Boija et al., 2018; Kwon et al., 2013; Lu et al., 2018; Sabari et al., 2018) and adaptative stress  
55 responses (Franzmann and Alberti, 2019; Franzmann et al., 2018; Riback et al., 2017). Protein  
56 phase separation can occur at DNA damage sites. Upon laser micro-irradiation, the activity of  
57 poly(ADP-ribose) polymerase 1 seeds the condensation of the prototypical liquid-liquid phase  
58 separation protein FUS at damaged chromatin (Altmeyer et al., 2015; Patel et al., 2015). 53BP1  
59 phase separates at double-strand DNA breaks (Kilic et al., 2019; Pessina et al., 2019), and the  
60 condensation of 53BP1 promotes induction of p53 and p21 (Kilic et al., 2019).

61 To explore the mechanisms and functional consequences of biomolecular condensates in  
62 the DNA damage response (DDR), we studied Topoisomerase II $\beta$ -binding protein (TopBP1), an  
63 essential factor in the DDR pathway and a prototype of protein scaffolds composed of multiple  
64 modular interaction domains. TopBP1 features nine repetitions of a well-folded protein-protein  
65 interaction motif, the BRCA1 C terminus domain (BRCT), and an ATR activation domain (AAD),  
66 located between BRCT6 and BRCT7, which is intrinsically disordered. TopBP1 brings together  
67 different sets of proteins to form distinct protein complexes involved in DNA replication initiation  
68 (Hashimoto and Takisawa, 2003; Makiniemi et al., 2001), DNA replication stress signalling  
69 (Kumagai et al., 2006; Mordes et al., 2008), DNA repair (Broderick et al., 2015; Leimbacher et  
70 al., 2019; Liu et al., 2017; Moudry et al., 2016) and transcription regulation (Liu et al., 2009;  
71 Wright et al., 2006). TopBP1 is the main activator of the master checkpoint kinase ATR (Kumagai  
72 et al., 2006; Mordes et al., 2008). ATR and its effector kinase Chk1 are crucial for cellular  
73 responses to DNA damage and DNA replication impediments (Ciccia and Elledge, 2010; Marechal  
74 and Zou, 2013; Saldivar et al., 2017). ATR/Chk1 signalling ensures cell and organismal survival

75 through coordination of DNA repair and DNA replication with physiological processes (Saldivar  
76 et al., 2017). Studies using *Xenopus* egg extracts have largely contributed to defining the  
77 orchestrated set of events leading to ATR activation (Acevedo et al., 2016; Byun et al., 2005;  
78 Duursma et al., 2013; Kumagai et al., 2006; Van et al., 2010). ATR is recruited to DNA lesions  
79 and replication intermediates via the ATR interacting protein ATRIP, which binds RPA-covered  
80 single-stranded DNA (Zou and Elledge, 2003). TopBP1 interacts with ATRIP, with ATR and with  
81 the RAD9-RAD1-HUS1 (9-1-1) clamp and activates ATR (Delacroix et al., 2007; Duursma et al.,  
82 2013; Kumagai et al., 2006; Mordes et al., 2008; Yan and Michael, 2009). Here, we used the  
83 conceptual framework born from studies of biomolecular condensates to gain fresh insights into  
84 the activation mechanism of ATR/Chk1 signalling. Using a combination of optogenetic and  
85 biochemical approaches, we show that TopBP1 self-assembles extensively to yield functional  
86 biomolecular condensates, and that purified TopBP1 has an intrinsic capacity to undergo liquid  
87 phase separation. We provide evidence that TopBP1 self-organization into micron-sized  
88 compartments in living cells activates ATR/Chk1 signalling and slows down the progression of  
89 replication forks. Our data indicate that essential responses to DNA replication impediments  
90 emerge from TopBP1-driven assembly of nuclear condensates.

91 **Results**

92 **TopBP1 drives the formation of micron-sized nuclear condensates.**

93 TopBP1 forms nuclear foci upon entry into mitosis (Leimbacher et al., 2019; Pedersen et al., 2015),  
94 and in cells exposed to hydroxyurea, ultraviolet light or ionizing radiations (Cescutti et al., 2010;  
95 Greer et al., 2003). To probe the capacity of TopBP1 to self-organize into biomolecular  
96 condensates, we fused TopBP1 to cryptochrome 2 (Cry2) of *Arabidopsis thaliana*, a protein that  
97 oligomerises upon exposure to 488nm light and seeds the formation of biomolecular condensates  
98 (Bugaj et al., 2013; Kilic et al., 2019; Shin et al., 2017; Zhang et al., 2019) (Figure 1A). This  
99 optogenetic system allows to control the nucleation of biomolecular condensates in space and time  
100 (Bracha et al., 2018; Shin et al., 2017; Shin et al., 2018), and evaluate the functional consequences  
101 of protein condensation (Kilic et al., 2019; Sabari et al., 2018). We induced the expression of  
102 TopBP1 fused to mCherry and Cry2 (named opto-TopBP1) with doxycycline in Flp-In HEK293  
103 cells. Overall, the expression level of recombinant opto-TopBP1 was similar to the level of  
104 endogenous TopBP1 (Figure S1A). At this level of expression, opto-TopBP1 remained in a diffuse  
105 state and was not directly detectable by fluorescence microscopy (Figure 1B, light OFF panel).  
106 Upon exposure of these cells to an array of blue-light LEDs during 3 minutes of light-dark cycles  
107 (4s light followed by 10s dark), we observed multiple and distinct opto-TopBP1 foci in the nuclei,  
108 specifically (Figure 1B, light ON panel). By contrast, we did not detect any foci in blue-light  
109 exposed cells expressing the opto-module (mCherry-Cry2) alone, nor in cells expressing the  
110 checkpoint clamp subunit opto-RAD9 (RAD9-mCherry-Cry2) (Figure S1B).

111 A conserved tryptophane in the ATR activation domain of TopBP1 at position 1138 in *Xenopus*  
112 *Laevis*, 1147 in mice, and 1145 in human, is essential for the capacity of TopBP1 to activate ATR  
113 (Kumagai et al., 2006) (Zhou et al., 2013). In mice, the substitution of W1147 for an arginine

114 residue is embryonic lethal, indicating that the ATR-activating function of TopBP1 is essential  
115 (Zhou et al., 2013). The W1148R substitution does not disrupt the association of xTopBP1 with  
116 xATR (Kumagai et al., 2006). Here, we analyzed the impact of W1145R on the capacity of  
117 TopBP1 to assemble higher order structures. W1145R TopBP1 expressing cells exhibited a  
118 markedly reduced number of optogenetic TopBP1 condensates in comparison with wild-type  
119 TopBP1 (Figure 1B), suggesting that this aromatic residue plays an important role in TopBP1  
120 higher-order assembly or in the growth of TopBP1 condensates.

121 Ewing's tumor associated antigen 1 (ETAA1) is required for Chk1 basal activity and  
122 stability (Michelena et al., 2019), and for the regulation of mitotic ATR signalling (Bass and  
123 Cortez, 2019). Like TopBP1, ETAA1 is endowed with an intrinsically disordered ATR activation  
124 domain (AAD) (Bass and Cortez, 2019; Bass et al., 2016; Haahr et al., 2016; Lee et al., 2016).  
125 Considering the conserved function of these disordered AADs, we replaced the AAD of TopBP1  
126 with the AAD of ETAA1, and then tested the capacity of the chimeric opto-TopBP1<sup>ETAA1-AAD</sup>  
127 protein to form condensates. In comparison with TopBP1, the TopBP1<sup>ETAA1-AAD</sup> chimeric protein  
128 exhibited reduced capacity to form condensates (Figure 1C). Consistent with this, optogenetic  
129 activation of ETAA1 fused to Cry2 did not yield foci (Figure S1C). Moreover, the AAD of TopBP1  
130 did not form optogenetic condensates (Figure 1D). Collectively, these data indicate that TopBP1  
131 can self-assemble into micron-sized condensates and that the TopBP1 AAD has unique  
132 characteristic features that are necessary but not sufficient for TopBP1 higher-order assembly.

133

#### 134 **Optogenetic and endogenous TopBP1 condensates share similar properties.**

135 A three-dimensional analysis revealed that optogenetically-induced TopBP1 condensates have a  
136 spherical shape with an aspect ratio close to one (Figure 2A + Suppl. video), suggesting that the

137 interface of these structures may be subjected to surface tension. Opto-TopBP1 condensates  
138 occasionally fused, hence TopBP1 can undergo dynamic clustering (Figure 2B). These structures  
139 dissolved within 15 minutes (Figure 2C + Figure S2A), while Cry2 oligomers disassemble  
140 spontaneously within 1-2 minutes (Shin et al., 2017). The relative stability of opto-TopBP1  
141 condensates reflects the role of TopBP1 multivalent cooperative interactions in the formation of  
142 micron-sized protein assemblies. Next, we assessed the permeability of TopBP1 condensates to  
143 the surrounding milieu by fluorescence redistribution after photobleaching. We expressed eGFP-  
144 TopBP1 in U-2-OS cells with doxycycline for 24 hours (Sokka et al., 2015). In these experimental  
145 conditions, overexpressed eGFP-TopBP1 spontaneously forms foci that accumulate in nucleoli  
146 (Sokka et al., 2015). After photobleaching, eGFP-TopBP1 bodies recovered fluorescence signal  
147 within seconds, which reflects the rapid exchange of eGFP-TopBP1 molecules between the  
148 nucleoplasm and TopBP1 nuclear condensates (Figure S2B). We conclude that the boundaries of  
149 TopBP1 compartments are permeable. We noted also that eGFP-TopBP1 bodies were sensitive to  
150 hexanediol (Figure S2C), an aliphatic alcohol that disrupts weak hydrophobic interactions  
151 (Kroschwald et al., 2017).

152         The cooperative interactions that drive the formation of biomolecular condensates are  
153 influenced by the properties of the surrounding milieu. Changes in osmotic concentration by  
154 addition of sorbitol or sucrose in the cell culture medium disrupt 53BP1 phase separation (Kilic,  
155 2019). Likewise, osmotic stress inhibited both the assembly of TopBP1 condensates induced by  
156 optogenetic activation (Figure 2D + Figure S2D), and the formation of endogenous TopBP1 foci  
157 induced by treatment with the inhibitor of ribonucleotide reductase hydroxyurea (Figure 2E +  
158 Figure S2E). This suggests that electrostatic forces drive the assembly of both synthetic  
159 (optogenetic) and endogenous TopBP1 condensates. Recombinant opto-TopBP1 also formed

160 nuclear foci in cells exposed to hydroxyurea (Figure S2F), indicating that like endogenous  
161 TopBP1, opto-TopBP1 engages with endogenous components in response to stalled replication  
162 forks. Whereas TopBP1 condensates appear as homogenous structures by conventional  
163 fluorescence microscopy, stimulated emission depletion (STED) nanoscopy with an anti-mCherry  
164 antibody revealed the underlying sub-structure of optogenetic TopBP1 condensates, which consist  
165 in clusters of spherical, nanometer-sized particles (Figure 2F, left panel). TopBP1 clusters had a  
166 very tight appearance when detected with an anti-TopBP1 antibody that recognizes both  
167 endogenous and recombinant TopBP1 (Figure 2F, right panel). Likewise, high-resolution imaging  
168 of endogenous TopBP1 in cells treated with hydroxyurea revealed numerous sub-structured  
169 clusters of nano-condensates (Figure 2G). The data suggest that whether seeded by DNA  
170 replication impediments or Cry2 oligomerisation, the driving forces and the organization of  
171 TopBP1 nuclear condensates are similar.

172

### 173 **TopBP1 undergoes liquid-liquid phase separation *in vitro*.**

174 To test if TopBP1 has the capacity to phase separate, we expressed and purified the carboxy-  
175 terminal half of TopBP1 (amino acids 884-1522). This portion of TopBP1, hereafter called b6-8,  
176 includes the BRCT 6 to 8 and the AAD (Figure 3A + Figure S3B). TopBP1<sup>b6-8</sup> mediates directly  
177 the activation of ATR, independently of its amino-terminal portion (Hashimoto et al., 2006;  
178 Kumagai et al., 2006). TopBP1<sup>b6-8</sup> formed optogenetically-induced foci in live cells (Figure S3A).  
179 In the presence of the crowding agent Polyethylene Glycol (2%), purified TopBP1<sup>b6-8</sup>-GFP formed  
180 spherical condensates detected by fluorescence microscopy (Figure 3B, upper panel and Figure  
181 S3C). Consistent with optogenetic experiments (Figure 1B), the W1145R substitution abolished  
182 the phase separation of TopBP1<sup>b6-8</sup> (Figure 3B, lower panel). Addition of TopBP1<sup>b6-8</sup>-RFP to pre-

183 formed TopBP1<sup>b6-8</sup>-GFP condensates yielded yellow compartments, indicating that soluble  
184 TopBP1 molecules are recruited to TopBP1 condensates. By contrast, W1145R TopBP1<sup>b6-8</sup>-RFP  
185 did not stably associate with TopBP1<sup>b6-8</sup>-GFP condensates (Figure 3C). TopBP1 condensates were  
186 permeable to DNA, as revealed by the partitioning of double-strand DNA fragments into pre-  
187 formed TopBP1 condensates (Figure 3D). In the presence of a circular DNA plasmid (2.9 kb),  
188 TopBP1<sup>b6-8</sup>-GFP formed clusters of nano-condensates that were reminiscent, yet not equivalent,  
189 to high-resolution images of cellular TopBP1 condensates (Figure 3E). This observation suggests  
190 that the long anionic DNA polymer strongly influences the assembly of TopBP1 molecules. In the  
191 absence of PEG, purified TopBP1<sup>b6-8</sup>-GFP (10 $\mu$ M) did not phase separate (Figure 3B minus PEG,  
192 and 3F). To recapitulate partially the complex environment of the nucleus, we spiked “Dignam  
193 and Roeder” nuclear extracts with recombinant TopBP1<sup>b6-8</sup>-GFP in physiologic salt concentration  
194 and pH. After incubation of the reaction mixture at 37°C, fluorescence microscopy analyses  
195 revealed  $\mu$ m-scaled TopBP1<sup>b6-8</sup>-GFP condensates (Figure 3F) co-localizing with endogenous  
196 DNA (Figure S3D). Hence, TopBP1 foci-like structures that depend on the integrity of the AAD  
197 are recapitulated with purified TopBP1 in the presence of a crowding agent or nuclear extracts.  
198 We conclude that TopBP1 has intrinsic capacity to form micron-sized condensates, both *in vitro*  
199 and in living cells.

200

### 201 **Consequence of TopBP1 condensation on TopBP1-associated protein network.**

202 To test if recombinant TopBP1 condensates mimic endogenous TopBP1 foci, we analyzed the  
203 composition of TopBP1 condensates assembled in live cells. We used a biotin labelling approach  
204 to gain a panoramic view of TopBP1 proximal proteins. A doxycycline-inducible cDNA encoding  
205 WT or W1145R TopBP1 fused to the mutated biotin ligase BirA\* and the Flag epitope was stably

206 integrated in Flp-In HEK293 cells (Figure 4A). We overexpressed Flag-BirA\*-TopBP1 to a level  
207 that induces constitutive BirA\*-TopBP1 condensates (Figure S4), in the absence of DNA  
208 damaging agents. We labelled TopBP1 proximal proteins with biotin for 3 hours. More than 500  
209 TopBP1 proximal proteins were identified by mass spectrometry with high confidence and  
210 reproducibility (Supplemental Excel sheet). Proteins were ranked according to their iBAQ value  
211 (intensity-based absolute quantification), a proxy for protein abundance (Figure 4B). Among  
212 abundant TopBP1 proximal proteins, we identified known TopBP1 partners, including TOP2A,  
213 FANCI, BRCA1, MRE11, MDC1, 53BP1 and BLM (Figure 4B). Only five proteins showed  
214 differences in abundance between WT and W1145R TopBP1 ( $\text{Log}_2 \text{diff} > 2$  with a  $p\text{-value} \leq 0.05$ )  
215 (Figure 4C). Among them, only the nucleolar protein NOL11 was detected at high level, and,  
216 therefore, considered as a significant difference between WT and W1145R TopBP1. This is  
217 consistent with a previous report demonstrating that upregulated TopBP1 accumulates on  
218 ribosomal chromatin, segregates nucleolar components and yields nucleolar caps (Sokka et al.,  
219 2015). By contrast, W1145R substitution abrogates TopBP1 nucleolar segregation (Sokka et al.,  
220 2015). Consistent with this, W1145R TopBP1 had lost proximity with the nucleolar protein  
221 NOL11 (Figure 4D). Immunoblot analysis of TopBP1 proximal proteins confirmed that the  
222 substitution W1145R in the AAD of TopBP1 does not alter the proximity of TopBP1 with partner  
223 proteins implicated in ATR signalling, including ATR, BRCA1, MRE11 and FANCI (Figure 4D).  
224 More generally, W1145R did not alter significantly the network of TopBP1 proximal proteins. In  
225 conclusion, at a low temporal resolution, whereas the composition of recombinant TopBP1  
226 assemblies recapitulates endogenous TopBP1 foci, TopBP1 condensation does not increase  
227 significantly the association of TopBP1 with partner proteins.  
228

229 **Functional consequences of TopBP1 condensation.**

230 In response to DNA replication impediments, ATR activates the effector checkpoint kinase 1  
231 (Chk1) by phosphorylation on Ser345. To establish a functional link between TopBP1  
232 condensation and ATR/Chk1 signalling, we exposed a cell culture dish to an array of blue-light  
233 LEDs for 3 minutes and then probed cell extracts for ATR mediated Chk1 phosphorylation on  
234 Ser345 by western blotting. Optogenetic condensation of TopBP1 induced robust phosphorylation  
235 of Chk1 Ser345 (Figure 5A) and of TopBP1 on Ser1138 (Figure 5B, t3), within 3 minutes, in the  
236 absence of an exogenous source of DNA damage. By contrast, the clustering defective W1145R  
237 TopBP1 mutant protein did not activate ATR/Chk1 signalling (Figure 5A). Consistent with the  
238 reversible dissolution of optogenetically-induced TopBP1 foci, phospho-Chk1 (Ser345)  
239 immunoblotting signals disappeared 20 minutes after optogenetic activation (Figure 5B, t23). Re-  
240 activation of TopBP1 condensates with blue light re-induced Chk1 phosphorylation (Figure 5B,  
241 t26), until dissolution of the reactivated TopBP1 condensates (Figure 5B, t46). We reiterated the  
242 process four times (Figure 5B). The data indicate that Chk1 activation by ATR intersects precisely  
243 with TopBP1 condensation, suggesting that TopBP1 condensation operates as a switch-like  
244 mechanism that amplifies ATR activity above a threshold required for Chk1 phosphorylation.

245 Of note, we observed the spontaneous activation of endogenous Chk1 in “Dignam and  
246 Roeder” nuclear extracts after 10 minutes incubation at 37°C (Figure S5A), in the absence of  
247 recombinant TopBP1 protein and without an exogenous ATR-activating DNA structures. The  
248 level of phospho Chk1 (Ser345) signals was significantly higher than background signals observed  
249 when reaction mixtures were incubated at 4°C, or at 37°C in the presence of the ATR and mTOR  
250 inhibitor ETP-46464 (Figure S5A), confirming that the reaction was the product of ATR activity  
251 and occurred *in vitro*. Phosphorylation of Chk1 was blocked when nuclear extracts were pre-

252 incubated with ethidium bromide, which disrupts protein-DNA interaction (Figure S5B),  
253 indicating that endogenous DNA fragments present in the extracts are required for ATR activation.  
254 The activation of endogenous ATR in nuclear extracts suggests that when a critical concentration  
255 of reactants is reached, a productive supramolecular ATR signalling complex assembles  
256 spontaneously.

257       Once activated by ATR through Ser345 phosphorylation, Chk1 auto-phosphorylates on  
258 Ser296. This step is required for Chk1 to induce downstream molecular events leading to cell cycle  
259 arrest (Kasahara et al., 2010). Light-induced TopBP1 condensation yielded Chk1 Ser296 phospho-  
260 signals, confirming that Chk1 is active (Figure S6A). UCN-01, an inhibitor of Chk1, blocked Chk1  
261 auto-phosphorylation on Ser296, but had no major impact on Chk1 phosphorylation on Ser345 by  
262 ATR (Figure S6A). This confirms that the Chk1 phospho Ser296 signal is a product of Chk1  
263 activity. To explore further the impact of TopBP1 condensation on the interaction of TopBP1 with  
264 partner proteins, we took advantage from the optogenetic tool shown in Figure 1A. The TopBP1-  
265 mCherry-Cry2 used for light-induced foci formation was tagged at its N-terminus with TurboID,  
266 an optimized biotin ligase that can biotinylate proteins within minutes (Branon et al., 2018). To  
267 detect ATR activity within optogenetic TopBP1 condensates, we induced TopBP1 condensation  
268 by 488 nm light in the presence of biotin in the cell culture medium, and then purified biotinylated  
269 proteins with streptavidin-coated beads. We enriched phospho ATR (Thr1989) and phospho  
270 TopBP1 (Ser1138) signals from cells expressing WT TopBP1 after optogenetic activation,  
271 specifically (Figure 5C). Furthermore, this biotin labelling strategy allowed to capture some Chk1  
272 phosphorylation events occurring within TopBP1 condensates (Figure S6B). By contrast, we did  
273 not isolate biotinylated phospho ATR, phospho TopBP1 and phospho Chk1 in proximity to  
274 W1145R TopBP1 (Figure 5C and Figure S6B). These data indicates that the condensation of

275 TopBP1 promotes the phosphorylation of ATR target proteins. In fluorescence microscopy,  
276 optogenetic TopBP1 condensates co-localised with RAD9 and with phospho ATR (Figure S6C-  
277 D). By contrast, Chk1 Ser345 phospho-signals rarely co-localised with TopBP1 condensates *per*  
278 *se*, but were detected in cells positive for TopBP1-mCherry condensates (Figure S6E), consistent  
279 with Chk1 high mobility (Liu et al., 2006). Chk1 is not retained physically at DNA damage sites,  
280 allowing signal transmission from DNA damage sites to the rest of the cell (Liu et al., 2006).  
281 Super-resolution STED imaging revealed phospho ATR (Thr1989) signals intertwined with  
282 TopBP1 nano-condensates in TopBP1 clusters (Figure 5D). These observations indicate that  
283 TopBP1 condensates function as reaction hubs.

284         As optogenetic TopBP1 condensates were chromatin bound (Figure S6F), we analyzed the  
285 consequences of TopBP1 condensation on the progression of DNA replication forks using a DNA  
286 fiber labelling approach. We induced TopBP1 condensation during the CldU pulse using two  
287 cycles of 3 minutes blue-light illumination, in order to actuate and maintain TopBP1 foci during  
288 the 20 minutes labelling period (Figure 5E). DNA replication tracks labelled in the presence of  
289 optogenetic TopBP1 condensates were shorter than DNA replication tracks labelled in the absence  
290 of optogenetic activation. By contrast, blue-light illumination did not alter the progression of  
291 replication forks in cells that express the condensation defective mutant W1145R TopBP1. We  
292 conclude that TopBP1 condensates are functional entities. Mechanistically, TopBP1 condensation  
293 triggers activation of ATR/Chk1 signalling.

294

### 295 **Regulation of TopBP1 condensation**

296 TopBP1 is highly phosphorylated in response to DNA replication stress (Munk et al., 2017), and  
297 the activation of ATR/Chk1 signalling is dependent on TopBP1 phosphorylation (Burrows and

298 Elledge, 2008; Hashimoto et al., 2006; Yoo et al., 2007). We reasoned that the basal kinase activity  
299 of ATR, which is independent of TopBP1 (Liu et al., 2011), may play a role in the condensation  
300 process. To test this, we pre-incubated cells with the ATR inhibitors VE-821 (Charrier et al., 2011),  
301 or ETP-46464 (Llona-Minguez et al., 2014), for 1 hour, and then exposed opto-TopBP1 expressing  
302 cells to blue light for 3 minutes. In these experimental conditions, the formation of TopBP1  
303 condensates was inhibited and the phosphorylation of Chk1 on the ATR site Ser345 was blocked  
304 (Figure 6A + Figure S7A). By contrast, pre-incubation of the cells with the Chk1 inhibitor UCN-  
305 01 did not affect the formation of optogenetic TopBP1 condensates (Figure S7B). To explore  
306 further the role of ATR in TopBP1 condensation, we mutated key amino acids in the AAD (Figure  
307 6B). We substituted TopBP1 phenylalanine at position 1071 with alanine. This substitution locates  
308 within a predicted coiled coil in TopBP1 AAD and partially destabilizes the interaction of TopBP1  
309 with ATR (Thada and Cortez, 2019). The F1071A substitution severely reduced the optogenetic  
310 induction of TopBP1 condensates (Figure 6C, left panel + Figure S7C). Biotin labelling revealed,  
311 however, that F1071A TopBP1 remained proximal to ATR and basal phosphorylation on Ser1138  
312 was detected (Figure 6D). The Ser1138 phospho signal was induced upon optogenetic activation  
313 of WT TopBP1 condensates, but not in cells expressing F1071A TopBP1, consistent with a  
314 condensation defect (Figure 6D). Several contact points maintain TopBP1 in proximity with the  
315 ATR-ATRIP complex (Thada and Cortez, 2019). Hence, the reduction of the strength of the  
316 association of F1071A TopBP1 with ATR-ATRIP does not fully account for the severe  
317 condensation defect observed in these experimental conditions (Figure 6C).

318 In *Xenopus Laevis*, the phosphorylation of Ser1131 enhances the capacity of TopBP1 to activate  
319 ATR (Yoo et al., 2009). XTopBP1Ser1131 corresponds to Ser1138 in human TopBP1. Ser1138A  
320 partially inhibited the optogenetic activation of TopBP1 condensates, whereas the phospho mimic

321 S1138D stimulated TopBP1 condensation (Figure 6C, left panel + Figure S7C). The partial  
322 suppression of TopBP1 condensates by S1138A suggests that additional phospho-sites contribute  
323 to the cooperative assembly of TopBP1 condensates. In blue-light exposed cells expressing  
324 F1071A TopBP1 or S1138A TopBP1, the level of Chk1 phosphorylation on Ser345 was reduced  
325 in comparison with cells expressing WT TopBP1 (Figure 6C, right panel). Furthermore, phospho  
326 Ser1138 TopBP1 and phospho Thr1989 ATR signals were barely detectable in streptavidin  
327 pulldowns (Figure 6D). By contrast, the phosphomimetic substitution S1138D in TopBP1 yielded  
328 phospho Ser345 Chk1 signals upon optogenetic activation (Figure 6C, right panel) and phospho  
329 Thr1989 ATR was enriched in proximity of TopBP1 (Figure 6D). Collectively, the data suggest  
330 an amplification mechanism for activation of ATR/Chk1 signalling, whereby TopBP1  
331 phosphorylation by ATR induces TopBP1 condensation, and TopBP1 condensation unleashes its  
332 capacity to activate ATR.

## 333 **Discussion**

334 In this study, we provide evidence that TopBP1 is a protein scaffold that can self-assemble  
335 extensively to yield tight clusters of nano-condensates, and that the association of TopBP1 with  
336 ATR yields a positive feedback loop. We propose that TopBP1 condensation is a molecular switch  
337 that triggers checkpoint responses to DNA replication impediments. TopBP1 condensation  
338 depends on the basal kinase activity of ATR and on the phosphorylation of TopBP1 on serine  
339 1138. Thus, we propose a refined model of ATR activation (Figure 7). In the early stages of ATR  
340 signalling, ATR-ATRIP and TopBP1 congregates on RPA-coated single-stranded DNA, the 9-1-  
341 1 complex is loaded at single to double strand DNA junctions and stabilizes TopBP1. In later  
342 stages, the phosphorylation of TopBP1 induces its higher-order assembly into micron-sized  
343 clusters of nano-condensates that propel ATR signal transduction. The yeast homologue of ATR,  
344 Mec1, has been proposed to be activated via an allosteric mechanism (Wang et al., 2017). We  
345 surmise that the compartmentation of ATR signalling proteins creates a reaction hub where the  
346 probability of molecular interactions required for ATR activation is increased. A TopBP1  
347 clustering mechanism for ATR activation is reminiscent of Ras clusters that assemble transiently  
348 on the plasma membrane, and function as high-gain amplifiers critical for MAPK signal  
349 transduction (Prior et al., 2003; Tian et al., 2007).

350 The data shown here suggest that the molecular forces driving TopBP1 condensation are  
351 multiple weak and highly cooperative interactions. First, whether seeded by hydroxyurea-induced  
352 replication stress or Cry2 oligomerisation, TopBP1 nuclear condensates were dissolved upon  
353 addition of sorbitol or sucrose in the cell culture medium. These compounds destabilize weak  
354 electrostatic interactions involved in protein phase separation. The aliphatic alcohol hexanediol  
355 also dissolves TopBP1 condensates, suggesting that hydrophobic interactions contribute to

356 TopBP1 higher order assembly. Second, purified TopBP1 undergoes liquid-liquid phase  
357 separation, a characteristic feature of multivalent protein scaffolds that underpin the formation of  
358 membrane-less compartments. TopBP1 phase separation *in vitro* occurred also in the complex  
359 environment of a nuclear extract, where multiple homotypic and heterotypic interactions could  
360 influence the capacity of TopBP1 to self-assemble. Third, TopBP1 condensation was highly  
361 sensitive to key amino acids substitutions and post-translational modifications in the AAD. These  
362 modifications typically change the cooperative molecular forces that organize protein  
363 condensation. Last, our results suggest that the BRCT6-8 also contributes to TopBP1 higher-order  
364 assembly, consistent with data showing that BRCT7/8 promotes TopBP1 oligomerisation  
365 (Chowdhury et al., 2014). We observed that both optogenetic and endogenous TopBP1 form tight  
366 clusters of nano-condensates. Interestingly, in mitosis, TopBP1 forms filamentous structures that  
367 bridge MDC1 foci (Leimbacher et al., 2019), suggesting that specific molecular associations  
368 dictate the organization of TopBP1 higher-order structures.

369         The function of TopBP1 condensation described here explains previous observations. In  
370 *Saccharomyces cerevisiae*, artificial co-localization of the 9-1-1 complex and Ddc2<sup>ATRIP</sup>-Mec1<sup>ATR</sup>  
371 via tethering to an array of 256 LacO repeats bypasses the requirement for DNA damage to activate  
372 Mec1<sup>ATR</sup> (Bonilla et al., 2008). In *Schizosaccharomyces pombe*, artificial tethering of either one  
373 of Rad3<sup>ATR</sup>, RAD4<sup>TopBP1</sup> or RAD9 to a LacO array triggers a checkpoint response that utilizes the  
374 endogenous proteins (Lin et al., 2012). Furthermore, TopBP1 activates ATR *in vitro* and in cells  
375 when artificially tethered to DNA (Lindsey-Boltz and Sancar, 2011). Based on the findings  
376 described here, we surmise that the artificial tethering of checkpoint proteins to LacO arrays is  
377 nucleating the condensation of endogenous proteins, which switches on checkpoint signalling.

378           The transient and reversible nature of the molecular forces that underpin the formation of  
379 functional TopBP1 nuclear condensates appears well adapted to cellular regulation and optimal  
380 responsivity to DNA replication impediments, as opposed to the stable interaction of proteins that  
381 characterize molecular machines with defined stoichiometry. The formation of functional micron-  
382 sized condensates through the regulated self-assembly of multivalent protein scaffolds may  
383 represent a fundamental principle underlying the formation of functional nuclear foci in response  
384 to DNA damage.

385

### 386 **Limitations**

387 We did not deplete endogenous TopBP1 in our tractable optogenetic system because the ATR-  
388 activating function of TopBP1 is essential. As TopBP1 self-interacts, we must consider that  
389 endogenous TopBP1 enters into the composition of optogenetic TopBP1 condensates, and may  
390 attenuate the impact of amino acids substitutions on the properties of recombinant TopBP1. This  
391 study does not reveal the underlying molecular organization of TopBP1 condensates. Accurate  
392 energetic and structural analyses will be necessary to understand how point mutations in the ATR  
393 activation domain affect the kinetics of TopBP1 condensation. Single molecule tracking and  
394 quantitative measurements of the dynamics of molecules at the interface between the dense and  
395 the dilute phases will give insights into the biophysical properties of TopBP1 condensates.

396 **Acknowledgments**

397 We thank all members of the laboratory, Olivier Ganier and Pierre-Henri Gaillard for their critical  
398 reading of the manuscript. We are grateful to Lee Zou for the cDNA encoding TopBP1, Brian  
399 Raught for pCDNA5\_FRT-TO\_FlagBirA\*, Clifford P Brangwynne for the cDNA encoding Cry2,  
400 Juhani E. Syväoja for the U-2-OS cell lines expressing eGFP-TopBP1 and Simon Alberti for  
401 technical information. This work was supported by la Fondation ARC pour la recherche sur le  
402 cancer (PGA1 RF20180206787), MSD Avenir, and the SIRIC Montpellier Cancer (grant  
403 INCa\_Inserm\_DGOS\_12553).

404

405 **Author contributions**

406 Conceptualization: C.F., J.B. and A.C; Methodology: C.F., J.B. and A.C.; Investigation: C.F.,  
407 A.P., S.V., E.A., M.L., M-P.B., S.U. and J.B.; Data curation: C.F., A.P. J.B and A.C. Writing-  
408 original draft: C.F., J.B. and A.C. Writing-Review & Editing: C.F., A.P., J.B. and A.C.  
409 Supervision: J.B. and A.C. Project Administration: A.C. Funding Acquisition: A.C.

410

411 **Declaration of Interests**

412 The authors declare no competing interests.

413 **Main Figure Legends**

414 **Figure 1. Optogenic activation of TopBP1 condensates.** **A)** Schematic representation of the  
415 TopBP1 optogenetic platform **B)** Optogenetic activation of wild-type and W1145R TopBP1. The  
416 opto-module denotes mcherry-Cry2. Light ON: 3 min cycles of 4s light (488nm)-10s resting.  
417 Representative fluorescence images are shown. DNA is stained with Hoechst 33258. Scale bars:  
418 10 $\mu$ m. Violin plot represents distribution of number of condensates per cell. Median and quartile  
419 values are represented by continuous and dashed lines, respectively. The statistical significance  
420 between samples is represented by \*. Number of biological replicates = 3. See Figure S1A for  
421 protein expression levels. **(C)** Optogenetic activation of opto-TopBP1<sup>ETAA1-AAD</sup>. **(D)** Optogenetic  
422 activation of opto-AAD-NLS<sup>TopBP1</sup>. FL stands for Full Length.

423

424 **Figure 2. Properties of TopBP1 condensates.** **A)** 3D analysis of opto-TopBP1 condensates by  
425 IMARIS software. Sphericity =  $\text{area}^{\text{sphere}}/\text{area}^{\text{particle}}$ . The 3D projection and the spherical value for  
426 particle 1 (P1) is represented. Other particles were analyzed for their spherical values  
427 (P2=0.932587; P3=0.918362; P4=0.949144; P5=0.935103). Scale bar: 2 $\mu$ m. **B)** Time laps  
428 microscopy images of activated opto-TopBP1 condensates. **C)** Histograms representing the mean  
429 of mCherry-labelled condensates per cell. Activated TopBP1 WT condensates were incubated in  
430 the dark for the indicated time. **(D)** Violin plot representing the number of optogenetic TopBP1  
431 condensates in cells were pre-treated with 0.5M sucrose or 0.4M sorbitol for 1h, as indicated. **(E)**  
432 Violin plot representing the number of endogenous TopBP1 foci per cell in cells treated with 5mM  
433 HU and 0.5M sucrose or 0.4M sorbitol, as indicated. The values correspond to the sum of three  
434 independent experiments. **C-D-E)** Number of biological replicates = 3. See Figure S2A, S2D and  
435 S2E for representative images. **F)** Representative super-resolution STED images of optogenetic

436 TopBP1 condensates identified with anti-mCherry (left panel) or anti-TopBP1 (right panel). **G)**  
437 STED image of endogenous TopBP1 induced by hydroxyurea (left panel). Right panel: untreated  
438 control cells. Scale bars: 2 $\mu$ m for CONFOCAL images and 1 $\mu$ m for STED images.

439

440 **Figure 3. Purified TopBP1<sup>b6-8</sup> phase separates.** **A)** Schematic representation of recombinant WT  
441 and W1145R TopBP1 (TopBP1<sup>b6-8</sup>), tagged with 6xHistidine and maltose binding protein (MBP)  
442 at the N-terminus, and monomeric Green Fluorescent Protein (GFP) at the C-terminus. PreScission  
443 (3C) and TEV protease sites are indicated. See Figure S3B for stain-free gel of recombinant  
444 proteins. **B)** Representative images of TopBP1 (10 $\mu$ M) incubated in physiological buffer and,  
445 when indicated, 2% PEG. Scale bars: 10 $\mu$ m. See also Figure S3C. **C-D)** Schematic and  
446 representative images of TopBP1<sup>b6-8</sup>-RFP (1 $\mu$ M) (**C**) and double-stranded DNA (300nM) (**D**)  
447 trapping by pre-formed TopBP1<sup>b6-8</sup>-GFP (10 $\mu$ M) droplets. DNA stained with Hoechst 33258 (**D**).  
448 Scale bars: 10 $\mu$ m. Line scan of GFP-RFP (**C**) and GFP-Hoechst (**D**) signals is used to analyze co-  
449 localisation. **E)** Confocal image of purified (2.5 $\mu$ M) WT TopBP1<sup>b6-8</sup> and 40ng 2.9 kb circular  
450 DNA plasmid DNA marked with Hoechst 33258. Scale bar: 2 $\mu$ m. **F)** Fluorescence microscopy  
451 image of condensates in suspension after incubation of purified (2 $\mu$ M) WT and W1145R  
452 TopBP1<sup>b6-8</sup> in nuclear extracts (0.2 $\mu$ g/ $\mu$ l). Control images of TopBP1<sup>b6-8</sup>-GFP (10 $\mu$ M) alone and  
453 of protein extract (0.2 $\mu$ g/ $\mu$ l) are shown. Scale bars: 10 $\mu$ m. See Figure S3D for co-localization with  
454 endogenous DNA. **B-C-D-E-F)** Number of biological replicates = 3.

455

456 **Figure 4. Composition of TopBP1 condensates.** **A)** Schematic representation of the Flag-BirA\*  
457 TopBP1 platform. See Figure S4 for representative images of BirA\*-TopBP1 condensates. **B-C)**  
458 Proteins identified by mass spectrometry were ranked according to their iBAQ value (**B**) or

459 compared in a Volcano plot (C). A standard t-test was used to evaluate differences in protein  
460 abundance between samples. **D)** Streptavidin pulldowns of proteins biotinylated by WT and  
461 W1145R Flag-BirA\*-TopBP1 were probed for the indicated proteins by immunoblotting. When  
462 indicated (+), expression of Flag-BirA\*-TopBP1 was induced with 1µg/ml doxycycline.

463

464 **Figure 5. TopBP1 condensation activates ATR/Chk1 signaling.** **A)** The indicated proteins were  
465 probed by immunoblotting after light activation of cells expressing the opto-module control, WT  
466 TopBP1 or W1145R TopBP1, as indicated. **B)** Reiterative activation of ATR/Chk1 signaling.  
467 Resting and optogenetic activation times are indicated in red and green, respectively. **C)**  
468 Streptavidin pulldowns of biotinylated proteins before and after optogenetic activation, as  
469 indicated. See Figure S6B for biotinylated phospho-Chk1 signal. **D)** Representative super-  
470 resolution STED image of opto-TopBP1 and pATR (Thr1989) fluorescent signals. Co-localisation  
471 is indicated by line scan. Scale bar: 1µm. **E)** Replication tracks were labelled with two consecutive  
472 20' pulses of CldU and IdU. Dot plots represent CldU/IdU incorporation ratio of cells expressing  
473 WT and W1145R opto-TopBP1, before (-) and after (+) optogenetic activation. Mean values are  
474 represented by red lines and the statistical significance among them is represented by \*. Number  
475 of biological replicates = 3.

476

477 **Figure 6. Regulation of TopBP1 condensation.** **A)** Impact of ATR inhibitors on TopBP1  
478 condensation. Violin plot represents the number of light-induced TopBP1 condensates in cells pre-  
479 treated with 10µM ATR inhibitors ETP-46464 or VE-822, as indicated. Cells used for optogenetic  
480 experiments were probed for the indicated proteins by immunoblotting. See Figure S7A for  
481 representative images. **B)** Alignment of ATR Activation Domain (AAD) sequences from Human,

482 Mouse and Xenopus. **C)** Violin plot represents the number of light-induced condensates in cells  
483 expressing the indicated mutant proteins. Cells were probed for the indicated proteins by  
484 immunoblotting. See Figure S7C for representative images. **D)** Streptavidin pulldowns of proteins  
485 biotinylated by WT or mutants opto-TopBP1 proteins were probed for the indicated proteins by  
486 immunoblotting. **A-C-D)** Number of biological replicates = 3.

487

488 **Figure 7. Model of ATR activation.** TopBP1 condensation enables ATR signal transduction.

489

490 **STAR Methods Text**

491 **RESOURCE AVAILABILITY**

492 ***Lead Contact***

493 Further information and requests for resources and reagents should be directed to and will be  
494 fulfilled by the Lead Contact, Angelos Constantinou ([angelos.constantinou@igh.cnrs.fr](mailto:angelos.constantinou@igh.cnrs.fr)).

495

496 ***Materials Availability***

497 Plasmids generated in this study are available upon request.

498

499

500 ***Data and Code Availability***

501 Original data for figures in the paper are available at Mendeley  
502 (<http://dx.doi.org/10.17632/6nf7b7ffb7.1>).

503

504 **EXPERIMENTAL MODEL AND SUBJECT DETAILS**

505 ***Human Cell lines***

506 *Flp-In<sup>TM</sup>T-REx<sup>TM</sup>293* and *HEK293* cell lines were grown under standard conditions (37°C, 5%

507 CO<sub>2</sub>) in Dulbecco's modified Eagle's medium (Merck-Sigma-Aldrich, D5796). For *Flp-In<sup>TM</sup>T-*

508 *REx<sup>TM</sup>293* the medium was supplemented with 10% fetal bovine serum (FBS), 100µg/ml Zeocin

509 and 15µg/ml Blasticidin. *Flp-In<sup>TM</sup>T-REx<sup>TM</sup>293* transfected cells were selected and maintained with  
510 15µg/mL Blasticidin and 150µg/mL Hygromycin.  
511 U-2-OS Tet-On cell lines expressing eGFP-TopBP1 WT and RPE1 cell lines were grown under  
512 standard conditions (37°C, 5% CO<sub>2</sub>) in modified McCoy's 5a medium (Merck-Sigma-Aldrich,  
513 M9309) supplemented with 10% fetal bovine serum (FBS), 100µg/ml of Hygromycin and  
514 200µg/ml of G418 as selective antibiotics (Sokka et al., 2015). Expression of eGFP-TopBP1 WT  
515 was induced with 1µg/ml of doxycycline for 24 hours.

516

### 517 *Sf9 insect cells*

518 Sf9 cells were grown in EX-CELL® 420 Serum-free medium (Sigma-Aldrich, 14420C). Cells  
519 were maintained between 2x10<sup>6</sup> and 1x10<sup>7</sup> cells/ml at 28°C in flasks (agitation 140 rpm).

520

## 521 **METHOD DETAILS**

### 522 *Plasmid constructs*

523 Oligonucleotides used for plasmids construction are listed in Supplementary Table S1. For  
524 pCDNA5\_FRT-TO\_Flag-BirA\*-TopBP1 WT or W1145R, TopBP1 full-length cDNA (a kind gift  
525 from Lee Zou) was amplified by PCR with primers 1 and 2 using Phusion® High-Fidelity DNA  
526 Polymerase (New England Biolabs, CM0530). The forward and reverse primers contain *AscI* and  
527 *NotI* sites, respectively. The amplified PCR was inserted into the pCDNA5\_FRT-TO\_Flag-BirA\*  
528 (a kind gift from Biran Raught) linearised with *AscI/NotI* digestion.

529 For pCDNA5\_FRT-TO\_mCherry-Cry2 (opto-module#), the Flag-BirA\* fragment was deleted  
530 from the pCDNA5\_FRT-TO\_FlagBirA\* using *KpnI/AscI* enzymes and replaced with the  
531 mCherry-Cry2 fragment amplified by PCR from the plasmid pHR-mCherry-Cry2 (a kind gift from

532 Brangwynne's lab) with primers 4 and 5. In the second step, TopBP1 amino acids 884 to 1522  
533 fragment (BRCT6-AAD-BRCT7-8 WT or W1145R) was amplified with primers 6 and 7, digested  
534 with *KpnI/NheI* and inserted into pCDNA5\_FRT-TO\_mCherry-Cry2 to produce opto-TopBP1<sup>b6-</sup>  
535 <sup>8</sup>WT and opto-TopBP1<sup>b6-8</sup>W1145R. For pCDNA5\_FRT-TO\_TurboID-mCherry-Cry2  
536 construction (opto-module), the TurboID fragment was amplified by PCR from the 3xHA-  
537 TurboID-NLS\_pCDNA3 plasmid (Addgene #107171) with primers 8 and 9, digested with  
538 *AflIII/KpnI* enzymes and inserted into the opto-module# to produce the opto-module. In the second  
539 step, TopBP1 WT and W1145R were amplified by PCR with primers 10 and 11, digested with  
540 *PmlI/KpnI* enzymes and inserted into the opto-module construct. Mutations in the AAD of TopBP1  
541 were generated using the “*QuickChange Multi Site-directed mutagenesis kit*” (Agilent  
542 technologies, C200515): W1145R with primer 3, F1071A with primer 12, S1138A with primer  
543 13, S1138D with primer 14. pCDNA5\_FRT-TO\_TurboID-AAD-NLS<sup>TopBP1</sup>-mCherry-Cry2 was  
544 generated by PCR amplification of TopBP1 AAD (primers 15-16) and TopBP1 NLS ( primers 17-  
545 18). Fragments were inserted in 2 steps into the opto-module digested with *AflIII/KpnI* (TopBP1  
546 AAD) and *KpnI/NheI* (TopBP1 NLS) enzymes respectively. pCDNA5\_FRT-TO\_TurboID-  
547 ETAA1-mCherry-Cry2 was generated by PCR amplification of ETAA1 with primers 19 and 20  
548 on pCDNA5\_FRT-TO \_GFP-ETAA1 (a kind gift from Mailand's lab) and insertion of the  
549 fragments into the opto-module digested with *KpnI/NheI* enzymes. pCDNA5\_FRT-TO\_TurboID-  
550 RAD9A-mCherry-Cry2 was generated by PCR amplification of RAD9 with primers 21 and 22 on  
551 pDONR223-RAD9A (obtained through MGC Montpellier Genetic Collections) and fragment was  
552 cloned into the *KpnI*-digested opto-module following the *In-Fusion HD Cloning Kit* protocol. The  
553 plasmid with the chimeric constructs of TopBP1 carrying the AAD of ETAA1 (pCDNA5\_FRT-  
554 TO\_TurboID-TopBP1<sup>ETAA1-AAD</sup>-mCherry-Cry2) was generated using the *NEBuilder HiFi DNA*

555 *assembly Master Mix* (New England Biolabs, E2621L). This kit was used to assemble multiple  
556 DNA fragments with 30 bp-overlap and replace 1530 bp inside TopBP1. DNA fragments were  
557 produced by PCR: oligos 23-24 were used to amplify TopBP1 sequence before the AAD (PCR on  
558 any plasmid containing full-length TopBP1), oligos 25-26 were specific for the AAD of ETAA1  
559 (PCR on pCDNA5\_FRT-TO\_GFP-ETAA1) and oligos 27-28 were specific for TopBP1 portion  
560 after the AAD (PCR on any plasmid containing full-length TopBP1). To obtain the chimeric  
561 constructs, PCR products were assembled according to the manufacturer's instruction and ligated  
562 into pCDNA5\_FRT-TO\_TurboID-TopBP1-mCherry-Cry2 digested with *EcoNI/SbfI*.  
563 pFastBac1 plasmids containing WT and W1145R BRCT 6 to 8 fragments of TopBP1 were  
564 synthesized by GeneScript after codon optimization for expression in insect cells (sequence  
565 available upon request), and sub-cloned into the 6His-MBP\_3C\_MCS\_TEV\_mRFP and 6His-  
566 MBP\_3C\_MCS\_TEV\_mGFP cassette using the restriction sites *EcoRI/KpnI*.

567

### 568 ***Western Blotting***

569 Whole cell extracts were lysed with 1X Laemmli Sample buffer (Biorad, C161-0737) and heated  
570 5min at 95°C. Cell extracts were resolved using pre-cast SDS-PAGE (7.5% and 10%) from BioRad  
571 and transferred to nitrocellulose membrane using a transfer apparatus according to the  
572 manufacturer's instructions (BioRad). Membranes were saturated with 10% non-fat milk diluted  
573 in TBS-0.2% Tween 20 (TBS-T), incubated with primary antibodies overnight at 4°C and with  
574 anti-mouse-HRP or anti-rabbit-HRP secondary antibodies for 1h. Blots were developed with ECL  
575 according to the manufacturer's instructions.

576

### 577 ***Affinity capture of biotinylated proteins: BioID***

578 *Flp-In<sup>TM</sup>T-REx<sup>TM</sup>293* cell lines stably transfected with Flag-BirA\*-TopBP1 WT or W1145R  
579 grown to 75% confluence were incubated with 1µg/ml of doxycycline (Clontech, 631311) for 16h  
580 and with 50µM biotin for 3 or 16 hours. Cells were washed with PBS and lysed with lysis buffer  
581 (50mM Tris-HCl pH 7.5, 150mM NaCl, 1mM EDTA, 1mM EGTA, 1% NP-40, 0.2% SDS, 0.5%  
582 Sodium deoxycholate) supplemented with 1X complete protease inhibitor (Roche) and 250U  
583 benzonase (Sigma, CE1014). Lysed cells were incubated on a rotating wheel for 1h at 4°C prior  
584 sonication on ice (40% amplitude, 3 cycles 10sec sonication- 2sec resting). After 30min  
585 centrifugation (7750 rcf) at 4°C, the cleared supernatant was transferred to a new tube and total  
586 protein concentration was determined by Bradford protein assay (BioRad, C500-0205). For each  
587 condition, 300µg of proteins were incubated with 30µl of Streptavidin-Agarose beads (Sigma,  
588 CS1638) on a rotating wheel at 4°C for 3hr. After 1min centrifugation (400 rcf), beads were  
589 washed, successively, with 1ml of lysis buffer, 1ml wash buffer 1 (2% SDS in H<sub>2</sub>O), 1ml wash  
590 buffer 2 (0.2% sodium deoxycholate, 1% Triton X-100, 500mM NaCl, 1mM EDTA, and 50mM  
591 Hepes pH 7.5), 1ml wash buffer 3 (250mM LiCl, 0.5% NP-40, 0.5% sodium deoxycholate, 1mM  
592 EDTA, 500mM NaCl and 10mM Tris pH 8) and 1ml wash buffer 4 (50mM Tris pH 7.5 and 50mM  
593 NaCl). Bound proteins were eluted from the magnetic beads using 80µl of 2X Laemmli Sample  
594 buffer and incubated at 95°C for 10min. 10% of the sample was used for Western blot analysis.  
595 For the *Flp-In<sup>TM</sup>T-REx<sup>TM</sup>293* cell lines stably transfected with the doxycycline-inducible TurboID-  
596 TopBP1WT-mCherry-Cry2 or the mutated forms of TopBP1, cells were simultaneously incubated  
597 with 500µM of biotin and exposed to blue light for 10min of light-dark cycles (4s light followed  
598 by 30s dark). Biotin proximity labelling of light-induced TopBP1 partners were pulled-down using  
599 streptavidin-coated beads as described before and probed by immunoblotting to detect proteins  
600 that are associated with TopBP1 clusters, in absence of DNA damage.

601

602 ***Mass Spectrometry***

603 Sample digestion was essentially performed as described (Shevchenko et al., 2006). Briefly,  
604 proteins were loaded on a SDS-PAGE (BioRad, 456-1034) and, after short migration, a single band  
605 was excised. Proteins in the excised band were digested with Trypsin (Promega, V5280). The  
606 resulting peptides were analyzed online by nano-flow HPLC-nanoelectrospray ionization using a  
607 Qexactive HFX mass spectrometer (Thermo Fisher Scientific) coupled to a nano-LC system  
608 (Thermo Fisher Scientific, U3000-RSLC). Desalting and preconcentration of samples were  
609 performed online on a Pepmap® precolumn (0.3 x 10mm; Fisher Scientific, 164568). A gradient  
610 consisting of 0% to 40% B in A (A: 0.1% formic acid [Fisher Scientific, A117], 6% acetonitrile  
611 [Fisher Scientific, A955], in H<sub>2</sub>O [Fisher Scientific, W6], and B: 0.1% formic acid in 80%  
612 acetonitrile) for 120min at 300nl/min was used to elute peptides from the capillary reverse-phase  
613 column (0.075 x 250mm, Pepmap®, Fisher Scientific, 164941). Data were acquired using the  
614 Xcalibur software (version 4.0). A cycle of one full-scan mass spectrum (375–1,500m/z) at a  
615 resolution of 60000 (at 200m/z) followed by 12 data-dependent MS/MS spectra (at a resolution of  
616 30000, isolation window 1.2m/z) was repeated continuously throughout the nanoLC separation.  
617 Raw data analysis was performed using the MaxQuant software (version 1.5.5.1) with standard  
618 settings. Used database consist of Human entries from Uniprot (reference proteome UniProt  
619 2018\_09) and 250 contaminants (MaxQuant contaminant database). Graphical representation and  
620 statistical analysis were performed using Perseus (version 1.6.1.1). A standard t-test was used to  
621 evaluate protein abundance difference between samples.

622

623 ***TopBP1 expression and purification***

624 Plasmids for protein expression in insect cells using baculoviruses are listed in Key Resources  
625 Table of Star Methods. For the production of bacmids, 50ng of pFastbac plasmids were  
626 transformed into MultiBac DH10 cells (Invitrogen, 10361-012) and positive clones were selected  
627 on LB Ampicilin (100µg/ml) plates supplemented with 40µg/ml IPTG, 100µg/ml XGal and  
628 7µg/ml Gentamycin. Blue colonies were screened for the presence of inserts by colony PCR using  
629 pUC/M13 Forward and Reverse oligos (Bac-to-Bac® Baculoviruses Expression  
630 System\_ *invitrogen user guide*). To generate baculoviruses,  $12 \times 10^6$  Sf9 cells (1ml) were transfected  
631 with 5µg of purified bacmid using 15µl of Cellfectin™ (Invitrogen, P/N 58760). After 5h  
632 incubation, 9ml of medium were added to Sf9 cells and cultures were incubated for 2.5 days. The  
633 supernatant (P1) was collected by centrifugation (400 rcf 10min) and a 1/100 dilution was used to  
634 infect  $4 \times 10^6$  cells/ml Sf9 cells. Cells were incubated for 2 days and the supernatant (P2) was  
635 collected by centrifugation. Expression of fluorescent proteins was verified by Western Blotting  
636 and microscopy. For protein expression, a 1/10 dilution of freshly prepared P2 was added to  $2 \times 10^6$   
637 cell/ml Sf9 culture and incubated for 48 to 72 hours.  
638 Infected cells were collected and lysed mechanically using a HTU-DIGI-French-Press (10000 PSI)  
639 in 15X packed cell weight hypertonic lysis buffer (50mM Na<sub>2</sub>H/NaH<sub>2</sub>PO<sub>4</sub> pH 8.0, 500mM NaCl,  
640 1% glycerol, 0.1% CHAPS) supplemented with protease inhibitors. Lysate was clarified by  
641 centrifugation (7750 rcf, 40min, 4°C), filtered and loaded on a 5ml HisTrap HP column (GE  
642 Healthcare, 71-5027-68 AF) equilibrated with 5CV (Column Volumes) of buffer A (lysis buffer +  
643 0.1 mM PMSF, 5mM imidazole). The column was washed with 5CV of buffer A and TopBP1<sup>b6-8</sup>  
644 was eluted stepwise using 5CV of buffer A + 30mM, 50mM, 75mM, 125mM and 500mM  
645 imidazole. Peak TopBP1<sup>b6-8</sup> fractions (eluted with 50mM and 75mM imidazole) were desalted  
646 (HiTrap™ or HiPrep 26/10, GE Healthcare) in physiological buffer (10mM Na<sub>2</sub>H/NaH<sub>2</sub> PO<sub>4</sub> pH

647 7.6, 150mM KOAc, 0.1mM MgOAc, 0.5mM DTT, 2.5% glycerol), snap frozen and stored at -  
648 80°C. Protein concentration was estimated by stain-free gel quantification using Image Lab  
649 Software.

650

### 651 *Nuclear extract preparation*

652 Nuclear extracts were prepared as previously described (Vidal-Eychenie et al., 2013). HeLa S3  
653 cells were grown to  $\leq 80\%$  confluence, collected by scrapping, centrifuged (200 rcf, 3min, 4°C)  
654 and washed twice in PBS 1X. Cell pellet was incubated on ice for 5min in 5X packed cell volume  
655 of hypotonic buffer A (10mM HEPES-KOH pH 7.9, 10mM KCl, 1.5mM MgCl<sub>2</sub>, 0.5mM DTT,  
656 0.5mM PMSF) supplemented with protease (complete, EDTA free; Roche, 31075800) and  
657 phosphatase inhibitors (Fisher Scientific). Cells were then spun down (500 rcf, 5min), suspended  
658 in 2X packed cell volume of buffer A and lysed by dounce homogenization using a tight-fitting  
659 pestle. Nuclei were collected by centrifugation (4000 rcf) for 5min at 4°C, extracted in one nuclei  
660 pellet volume of buffer C (20mM HEPES-KOH pH 7.9, 600mM KCl, 1.5mM MgCl<sub>2</sub>, 0.2mM  
661 EDTA, 25% glycerol, 0.5mM DTT, 0.5mM PMSF) supplemented with cocktails of protease and  
662 phosphatase inhibitors, and mixed on a rotating wheel at 4°C for 30min. Nuclear extracts  
663 (supernatants) were recovered by centrifugation (16000 rcf, 15min, 4°C) and dialyzed using Slide-  
664 A-Lyzer Dialysis Cassettes (3,500-D protein molecular weight cutoff; Fisher Scientific, 68035)  
665 against buffer D (20mM HEPES-KOH pH 7.9, 100mM KCl, 0.2mM EDTA, 20% glycerol, 0.5mM  
666 DTT, and 0.5mM PMSF). Dialyzed nuclear extracts were centrifuged (100000 rcf, 30min, 4°C) to  
667 eliminate residual precipitates. The protein concentration of the clear supernatant was determined  
668 by Bradford (BioRad, C500-0205) protein assay, and aliquots were snap frozen and stored at -

669 80°C. Important to note that the Dignam & Roeder extract preparation contain DNA fragments  
670 after centrifugation.

671

672 ***TopBP1 phase separation assay***

673 Phase separation of purified TopBP1<sup>b6-8</sup> was performed in physiological buffer C (10mM  
674 Na<sub>2</sub>H/NaH<sub>2</sub> PO<sub>4</sub> pH 7.6, 150mM KOAc, 0.1mM MgOAc, 0.5mM DTT, 2.5% Glycerol). Purified  
675 TopBP1<sup>b6-8</sup> WT and W1145R were digested with PreScission 3C enzyme (GenScript, Z03092-  
676 500) for 3h at 16°C to remove the 6-His and MBP tag before phase separation in reaction mixtures  
677 in buffer C containing 10µM of WT or W1145R TopBP1<sup>b6-8</sup>-GFP and 2% of PEG4000 (Merck-  
678 Sigma-Aldrich, 95904). Reaction mixtures were mixed by gently tapping the Eppendorf.

679 TopBP1 droplet permeability assay was performed in two steps: first, TopBP1<sup>b6-8</sup>-GFP droplets  
680 were formed in reaction mixtures containing 10µM of WT TopBP1<sup>b6-8</sup>-GFP supplemented with  
681 2% PEG in physiological buffer C, and then we added either 1µM of WT or W1145R TopBP1<sup>b6-8</sup>-  
682 RFP or *StuI/SacII* digested pX174 RFII DNA (300nM), as indicated. To study the role of DNA  
683 in the organization of TopBP1 condensates, we incubated 2.5µM of WT TopBP1<sup>b6-8</sup> with 40ng 2.9  
684 kb circular DNA plasmid DNA at 37°C during 10min in physiological buffer C. The ratio purified  
685 TopBP1:DNA was decided according to Choi JH et al., 2008. Samples were imaged on a LSM780  
686 confocal microscope (Leica, Germany) using a 63x oil immersion objective (N.A. 1.4). DAPI and  
687 GFP fluorescence were excited at 405 and 488nm respectively, and emitted fluorescence were  
688 collected sequentially at 415-460nm and 500-550nm respectively. The pinhole size was set to 1  
689 Airy unit.

690 TopBP1 phase separation in human protein extracts was performed in reaction mixtures containing  
691 0.2µg/µl of human nuclear extract, 2µM of WT or W1145R TopBP1<sup>b6-8</sup>-GFP in ATR activation

692 buffer (10mM Hepes-KOH pH 7.6, 50mM KCl, 0.1mM MgCl<sub>2</sub>, 1mM PMSF, 0.5mM DTT, 1mM  
693 ATP, 10µg/ml creatine kinase, 5mM phosphocreatine). Reaction mixtures were incubated for  
694 10min at 4°C or 37°C, as indicated. 5µl of reaction mixtures were used for analyses by  
695 immunofluorescence microscopy. Fluorescence microscopy analyses were performed using PEG  
696 silanized glass slides prepared as described (Alberti et al., 2018), and coverslips were sealed with  
697 nail polish. DNA was stained with Hoechst 33258. Images were captured on an inverted  
698 microscope using a 63x objective (NA 1.4 oil).

699

#### 700 ***Immunofluorescence staining***

701 Cells grown on coverslips were fixed with PBS/4% paraformaldehyde (PFA) for 15min at RT  
702 followed by a 10min permeabilization step in PBS/0.2% Triton X-100-PBS and blocked in  
703 PBS/3% BSA for 30min. For immunofluorescence staining, primary antibodies and appropriate  
704 secondary antibodies coupled to fluorochrome were diluted in blocking solution and incubated for  
705 1h at RT. To detect endogenous TopBP1, cells were pre-treated with Cytoskeleton (CSK) buffer  
706 before fixation. DNA was stained with Hoechst 33258 (Invitrogen, Cat H21491) and coverslips  
707 were mounted on glass slides with Prolong Gold antifade reagent (Invitrogen, Cat P36930). Images  
708 were captured using a 63x objective (NA 1.46 oil).

709

#### 710 ***Fluorescence Redistribution After Photo-bleaching (FRAP)***

711 For FRAP experiments, *U-2-OS Tet-On* cells were seeded into µ-Dish<sup>35 mm, high</sup> (Ibidi, 81156) and  
712 incubated 24h in the presence of 1µg/ml doxycycline to induce expression of eGFP-TopBP1.  
713 Imaging was realized using a 63x objective (NA 1.4). eGFP-TopBP1 bodies were photo-bleached

714 and the GFP signal intensity of 23 spots was measured before and during 5min following photo-  
715 bleaching with an imaging frequency of 60 images/min.

716

### 717 ***Opto-TopBP1 activation***

718 Cells were plated at around 70% confluency in DMEM. Expression of opto-TopBP1 was induced  
719 for 16h with 2µg/ml doxycycline. For light activation, plates were transferred into a custom-made  
720 illumination box containing an array of 24 LEDs (488nm) delivering 10mW/cm<sup>2</sup> (light intensity  
721 measured using a ThorLabs-PM16-121-power meter). Cry2 oligomerisation was induced using  
722 3min of light-dark cycles (4s light followed by 10s dark). Images were captured using a 63x  
723 objective (NA 1.46 oil). A Cell Profiler (version 2.2.0) pipeline was used to quantify nuclear  
724 mCherry foci. Values were represented via violin plots or histograms elaborated in Graph Pad  
725 Prism 8. Median and quartile values were indicated by continues and dashed lines respectively. A  
726 non-parametric t-test (Mann-Withney) was used to compare mCherry spot/cell distributions  
727 between samples. For each experiment, we performed three biological replicates and we show one  
728 representative experiment.

729

### 730 ***Live cell microscopy***

731 Live imaging of opto-TopBP1 WT overexpressing cells was performed on an inverted microscope  
732 (AxioObserver, Carl Zeiss, Germany) using a 63x oil immersion objective (NA 1.4). Fluorescence  
733 was detected on a CMOS camera (ORCA-Flash4.0, Hamamatsu) with an exposure time set to  
734 100ms and at frame rate of 2 images/min. All recordings were carried out at 37°C under 5% CO<sub>2</sub>.  
735 For Cry2 activation, cells were treated as explained before, under the microscope, and imaged  
736 immediately after light activation.

737

738 ***Stimulated emission depletion (STED) super-resolution microscopy***

739 For Figure 2F, *Flp-In<sup>TM</sup>T-REx<sup>TM</sup>293* cells expressing opto-TopBP1 were exposed to blue light  
740 (488nm) to induce TopBP1 foci, as described before. In Figure 2G, endogenous TopBP1 foci were  
741 analysed in *RPE1* cells after HU-induced replication stress (2h 5mM), untreated cells were used  
742 as control. For STED microscopy, immunolabelling of mCherry was realized using an anti-  
743 mCherry antibody followed by a secondary antibody coupled to Atto-647N fluorochrome.  
744 Confocal and STED imaging was performed using a quad scanning STED microscope (Expert  
745 Line, Abberior Instruments, Germany) equipped with a PlanSuperApo 100x/1.40 oil immersion  
746 objective (Olympus, Japan). Atto-647N was excited at 640nm with a dwell time of 10 $\mu$ s and STED  
747 was performed at 775nm. Images were collected in line accumulation mode (5 lines accumulation).  
748 Fluorescence was detected using avalanche photo diodes and spectral detection (650-750nm). The  
749 pinhole was set to 1.0 Airy units and a pixel size of 10nm was used for all acquisitions. A gating  
750 of 8ns was applied. Sphericity of opto-TopBP1 condensates was assessed using IMARIS software  
751 (Bitplane). For dual color STED imaging, Atto-647N and Abberior STAR Orange were used and  
752 respectively imaged at 640 and 561nm excitation. Detection was set to 650-750nm for Atto-647N  
753 and 570-630nm for Abberior STAR Orange. Other acquisition parameters were the same described  
754 as above.

755

756 ***DNA fibers***

757 Neo-synthesized DNA was sequentially pulse labelled with two halogenated thymidine analogs,  
758 5-Iodo-2'-deoxyuridine (IdU at 25 $\mu$ M – Sigma # I7125) and 5-Chloro-2'-deoxyuridine (CldU at  
759 50 $\mu$ M – Sigma # C6891), for 20min. After IdU incorporation, cells were washed two times before

760 CldU addition. CldU incorporation (20min total) was conducted in the presence of 3min of light-  
761 dark cycles (4s light followed by 10s dark) each 7min, to assure opto-TopBP1 condensates  
762 formation and persistence. Cells were trypsinized and washed with ice cold PBS. 2000 cells were  
763 drop on top of a microscope slide and let dry at least 5min before lyse with 7 $\mu$ L of spreading buffer  
764 (200mM Tris.HCl pH7.5, 50mM EDTA, 0.5% SDS) during 3min. DNA was spread by tilting the  
765 slide and letting the drop running down slowly. Once air-dry, DNA spreads were fixed in  
766 methanol/acetic acid 3:1 for 10min, denatured with 2.5M HCl during 1h and blocked in PBS/1%  
767 BSA/0.1% Tween. DNA spreads were immunostained with mouse anti-BrdU, rat anti-BrdU and  
768 mouse anti-ssDNA antibodies to detect IdU, CldU and intact DNA fibers respectively.  
769 Corresponding secondary antibodies conjugated to Alexa Fluor dyes were used in a second step.  
770 Images were captured using a 40x objective (NA 1.4 oil). The acquired DNA fiber images were  
771 analyzed by using FIJI Software and statistical analysis of at least 150 IdU and CldU tracks on  
772 intact fibers was performed with GraphPad Prism 8. Mean values were indicated by red lines. One-  
773 way ANOVA analysis was applied to compare means of samples in a group.

774

## 775 **QUANTIFICATION AND STATISTICAL ANALYSIS**

776 For Mass Spectrometry, raw data analysis was performed using the MaxQuant software  
777 (version 1.5.5.1) with standard settings. Graphical representation and statistical analysis were  
778 performed using Perseus (version 1.6.1.1). A standard t-test was used to evaluate protein  
779 abundance difference between samples.

780 Purified protein concentration was estimated by stain-free gel quantification using Image  
781 Lab Software (version 5.2.1).

782 All microscopy images were analyzed by OME Remote Objects (OMERO) software.  
783 Sphericity of opto-TopBP1 condensates was assessed using IMARIS software (Bitplane). STED  
784 microscopy and DNA fiber images were analyzed using FIJI software.

785 A Cell Profiler (version 2.2.0) pipeline was used to quantify nuclear mCherry foci.

786 All statistical analysis were performed with GraphPad Prism 8. For DNA fibers One-way  
787 ANOVA analysis was applied to compare means of samples in a group. To compare mCherry  
788 spot/cell distributions between samples we used a non-parametric t-test (Mann-Withney).

789

## 790 KEY RESOURCES TABLE

## 791 SUPPLEMENTAL INFORMATION

792 **Supplementary video. Related to Figure 2A.** 3D projection of opto-TopBP1 condensates.

793

794 **Table S1.** Oligonucleotides used in this study. Related to Key Resources Table and Method  
795 Details.

Primers	Sequence
Primer 1 (Fw)	TTGGCGCGCCAtccagaaatgacaaagaaccgt
Primer 2 (Rev)	TTTTCCTTTTGCGGCCGcttagtgactctaggtcgttg
Primer 3 (antisense)	GTAGGGTCATCCCTAATGATCTGTTCATTTTGGGAAGGC
Primer 4 (Fw)	GGGGTACCATCGATGCTAGCatggtgtctaaaggcgagga
Primer 5 (Rev)	GGCGCGCCtcagtcacgcattgacaggt
Primer 6 (Fw)	GGGGTACCACCATGctttctgccagccctca
Primer 7 (Rev)	CTAGCTAGCgtgtactctaggtcgtttgatt
Primer 8 (Fw)	gggCTTAAGgccaccATGaaagacaatactgtgcctctg
Primer 9 (Rev)	cggGGTACCCACGTGcttttcggcagaccgcaga
Primer 10 (Fw)	gggCACGTGtccagaaatgacaaagaaccg
Primer 11 (Rev)	cggGGTACCgtgtactctaggtcgtttgat
Primer 12 (sense)	gagatgagagagaacgctcagaagcagttacag
Primer 13 (sense)	gtcaacacagagcctgcccaaatgaacagatc
Primer 14 (sense)	gtcaacacagagcctgaccaaatgaacagatc
Primer 15 (Fw)	CTAGCGTTTAAACTTAAGATGgctgtgtcttcaaaaggatg

Primer 16 (Rev)	cctaCATGGTACCCatcatgtaaaggcttttgaaaagg
Primer 17 (Fw)	tacacGGTACCATGaggaaagctcctacag
Primer 18 (Rev)	caccatGCTAGCtctaggtcgttgatttta
Primer 19 (Fw)	AGCTTGGTACCATGAGTCGGCGAAGGAAACATGATG
Primer 20 (Fw)	ccgaaaagCACGTGGGTACCAAGTGCCTGGTCACGGG
Primer 21 (Rev)	atGCTAGCATCGATGGTACCGCCTTCACCCTCACTGTCTTCC
Primer 22 (Rev)	caccatGCTAGCAAGAAATGAAGTGGGAGCTGC
Primer 23 ( Fw )	tacacctggataccatcaaaattcctgtccaaggacaaac
Primer 24 (Rev)	CTTTGGTGTTCATAtgagagtagtcgactattacagagccg
Primer 25 ( Fw )	agtcgactactctcaTATGAAACACCAAAGAGAGCGCTGA
Primer 26 (Rev)	agcaatttctgaatcTGACCACATCTGTATATTATCTTTATAAATTAATTAATAAATCTCTGTTTCT
Primer 27 ( Fw )	ATACAGATGTGGTCAgattcagaaattgctaaacaggctgtct
Primer 28 (Rev)	ttcctgcacgaagtgtccagcagctcctgcaggcttcaaggta

796

## 797 **Supplementary Figure Legends**

798 **Figure S1. Related to Figure 1. A)** Immunoblotting of TopBP1. **B)** (Left) Representative  
799 fluorescence images of cells expressing opto-RAD9 under control of doxycycline. Light ON:  
800 488nm light. (Right) Immunoblotting of the cells with the indicated antibody. **C)** ETAA1 does not  
801 assemble condensates. The construct, representative fluorescence images, and Violin plot  
802 representation of quantified condensates are shown, as described in Figure 1.

803

804 **Figure S2. Related to Figure 2. A)** Representative fluorescence images of cells used for  
805 experiments in Figure 2C. DNA stained with Hoechst 33258. Scale bars: 10 $\mu$ m. **B)** (Left) FRAP  
806 recordings of two individual eGFP-TopBP1 condensates are reported as examples. Scale bars:  
807 10 $\mu$ m. (Right) Histogram representation of the mean of immobile and mobile fractions per nucleus  
808 (13 nuclei, 23 individual spots). **C)** Representative fluorescence images of eGFP-TopBP1

809 expressing U-2-OS cells treated, when indicated, with 3% of 1,6 Hexanediol. **D-E)** Representative  
810 fluorescence images of cells used for experiments in Figure 2D (**D**) and 2E (**E**). DNA stained with  
811 Hoechst 33258. Scale bars: 10 $\mu$ m. **F)** Violin plot representing the number of mCherry foci per cell  
812 in opto-TopBP1 expressing cells treated with 5mM HU. TopBP1 foci were identified with anti-  
813 mCherry antibody after CSK treatment. **A-B-C-D-E-F)** Number of biological replicates = 3.

814

815 **Figure S3. Related to Figure 3.** **A)** Representative fluorescence images of cells expressing opto-  
816 TopBP1<sup>b6-8</sup> WT before (Light OFF) and after (Light ON) optogenetic activation. DNA stained  
817 with Hoechst 33258. Western blotting of the indicated proteins is shown. Violin plot represents  
818 the number of mCherry foci per cell. **(B)** Stain-free gel of purified TopBP1<sup>b6-8</sup>-GFP WT and  
819 W1145R used for phase separation assays. **(C)** Representative fluorescence microscopy images of  
820 TopBP1 condensates assembled *in vitro*. The concentration of TopBP1 is indicated **(D)**  
821 Representative fluorescent images of TopBP1 condensates in suspension. DNA stained with  
822 Hoechst 33258. Line scan of GFP-Hoechst signals are shown. **A-C-D)** Scale bars: 10 $\mu$ m. Number  
823 of biological replicates = 3.

824

825 **Figure S4. Related to Figure 4.** Immunofluorescence staining of Flag-BirA\*-TopBP1 WT using  
826 anti-Flag antibody. Biotin conjugates were revealed using AlexaFluor streptavidin. DNA stained  
827 with Hoechst 33258. Scale bars: 10 $\mu$ m. Number of biological replicates = 3.

828

829 **Figure S5. Activation of endogenous ATR in nuclear extracts.** **A)** Nuclear extracts at the  
830 indicated protein concentration were incubated in the presence of the ATR inhibitor ETP-46464  
831 (10 $\mu$ M), as indicated. Chk1 activation is revealed by immunoblotting with the indicated

832 antibodies. \* represents unspecific bands. **B)** Immunoblotting of Chk1/pChk1 (Ser345) in reaction  
833 mixtures. When indicated nuclear extracts were pre-incubated with ethidium bromide (EtBr). **A-**  
834 **B)** Number of biological replicates = 3.

835

836 **Figure S6. Related to Figure 5.** **A)** Immunoblotting analyses of the indicated proteins before and  
837 after optogenetic activation of TopBP1 condensates. When indicated, cells were pre-treated with  
838 10 $\mu$ M UCN-01. **B)** Immunoblotting analysis of the indicated biotinylated proteins isolated with  
839 streptavidin beads in WT and W1145R opto-TopBP1 expressing cells exposed exposed to 488 nm  
840 light, when indicated. **C-D-E)** Immunofluorescence staining with the indicated antibodies of opto-  
841 TopBP1 expressing cells activated by light. Line scans are shown. DNA stained with Hoechst  
842 33258. Scale bars: 10 $\mu$ m. Violin plot (**E-right**) representing spot of pChk1 in cells with (dashed  
843 white line) or without (solid white line) opto-TopBP1 foci. **F)** Histograms representing the mean  
844 of mCherry foci per cell. Cells expressing opto-TopBP1 WT were exposed to 488 nm light, and,  
845 when indicated, nuclear soluble proteins were extracted with Cytoskeleton (CSK) buffer. **A-B-C-**  
846 **D-E-F)** Number of biological replicates = 3.

847

848 **Figure S7. Related to Figure 6.** **A)** Representative fluorescence images of cells used for  
849 optogenetic experiment in Figure 6A. **B)** Violin plot representing the number of mCherry  
850 condensates per cell in opto-TopBP1 expressing cells pre-treated for 1h with 10 $\mu$ M UCN-01, when  
851 indicated. **C)** Representative fluorescence images of cells used for optogenetic experiment in  
852 Figure 6C. **A-B-C)** Number of biological replicates = 3.

853

854 **References:**

855 Acevedo, J., Yan, S., and Michael, W.M. (2016). Direct Binding to Replication Protein A (RPA)-coated  
856 Single-stranded DNA Allows Recruitment of the ATR Activator TopBP1 to Sites of DNA Damage. *J Biol*  
857 *Chem* 291, 13124-13131.

858 Alberti, S., Saha, S., Woodruff, J.B., Franzmann, T.M., Wang, J., and Hyman, A.A. (2018). A User's Guide  
859 for Phase Separation Assays with Purified Proteins. *J Mol Biol* 430, 4806-4820.

860 Altmeyer, M., Neelsen, K.J., Teloni, F., Pozdnyakova, I., Pellegrino, S., Grofte, M., Rask, M.B., Streicher,  
861 W., Jungmichel, S., Nielsen, M.L., *et al.* (2015). Liquid demixing of intrinsically disordered proteins is  
862 seeded by poly(ADP-ribose). *Nat Commun* 6, 8088.

863 Banani, S.F., Lee, H.O., Hyman, A.A., and Rosen, M.K. (2017). Biomolecular condensates: organizers of  
864 cellular biochemistry. *Nat Rev Mol Cell Biol* 18, 285-298.

865 Bass, T.E., and Cortez, D. (2019). Quantitative phosphoproteomics reveals mitotic function of the ATR  
866 activator ETAA1. *J Cell Biol*.

867 Bass, T.E., Luzwick, J.W., Kavanaugh, G., Carroll, C., Dungrawala, H., Glick, G.G., Feldkamp, M.D., Putney,  
868 R., Chazin, W.J., and Cortez, D. (2016). ETAA1 acts at stalled replication forks to maintain genome  
869 integrity. *Nat Cell Biol* 18, 1185-1195.

870 Boija, A., Klein, I.A., Sabari, B.R., Dall'Agnesse, A., Coffey, E.L., Zamudio, A.V., Li, C.H., Shrinivas, K.,  
871 Manteiga, J.C., Hannett, N.M., *et al.* (2018). Transcription Factors Activate Genes through the Phase-  
872 Separation Capacity of Their Activation Domains. *Cell*.

873 Bonilla, C.Y., Melo, J.A., and Toczyski, D.P. (2008). Colocalization of sensors is sufficient to activate the  
874 DNA damage checkpoint in the absence of damage. *Mol Cell* 30, 267-276.

875 Bracha, D., Walls, M.T., and Brangwynne, C.P. (2019). Probing and engineering liquid-phase organelles.  
876 *Nat Biotechnol* 37, 1435-1445.

877 Bracha, D., Walls, M.T., Wei, M.T., Zhu, L., Kurian, M., Avalos, J.L., Toettcher, J.E., and Brangwynne, C.P.  
878 (2018). Mapping Local and Global Liquid Phase Behavior in Living Cells Using Photo-Oligomerizable  
879 Seeds. *Cell* 175, 1467-1480 e1413.

880 Branon, T.C., Bosch, J.A., Sanchez, A.D., Udeshi, N.D., Svinkina, T., Carr, S.A., Feldman, J.L., Perrimon, N.,  
881 and Ting, A.Y. (2018). Efficient proximity labeling in living cells and organisms with TurboID. *Nat*  
882 *Biotechnol* 36, 880-887.

883 Broderick, R., Nieminuszczy, J., Blackford, A.N., Winczura, A., and Niedzwiedz, W. (2015). TOPBP1  
884 recruits TOP2A to ultra-fine anaphase bridges to aid in their resolution. *Nat Commun* 6, 6572.

885 Bugaj, L.J., Choksi, A.T., Mesuda, C.K., Kane, R.S., and Schaffer, D.V. (2013). Optogenetic protein  
886 clustering and signaling activation in mammalian cells. *Nat Methods* 10, 249-252.

887 Byun, T.S., Pacek, M., Yee, M.C., Walter, J.C., and Cimprich, K.A. (2005). Functional uncoupling of MCM  
888 helicase and DNA polymerase activities activates the ATR-dependent checkpoint. *Genes Dev* 19, 1040-  
889 1052.

890 Cescutti, R., Negrini, S., Kohzaki, M., and Halazonetis, T.D. (2010). TopBP1 functions with 53BP1 in the  
891 G1 DNA damage checkpoint. *EMBO J* 29, 3723-3732.

892 Chowdhury, P., Lin, G.E., Liu, K., Song, Y., Lin, F.T., and Lin, W.C. (2014). Targeting TopBP1 at a  
893 convergent point of multiple oncogenic pathways for cancer therapy. *Nat Commun* 5, 5476.

894 Ciccio, A., and Elledge, S.J. (2010). The DNA damage response: making it safe to play with knives. *Mol*  
895 *Cell* 40, 179-204.

896 Delacroix, S., Wagner, J.M., Kobayashi, M., Yamamoto, K., and Karnitz, L.M. (2007). The Rad9-Hus1-Rad1  
897 (9-1-1) clamp activates checkpoint signaling via TopBP1. *Genes Dev* 21, 1472-1477.

898 Du, M., and Chen, Z.J. (2018). DNA-induced liquid phase condensation of cGAS activates innate immune  
899 signaling. *Science* 361, 704-709.

900 Duursma, A.M., Driscoll, R., Elias, J.E., and Cimprich, K.A. (2013). A role for the MRN complex in ATR  
901 activation via TOPBP1 recruitment. *Mol Cell* 50, 116-122.

902 Erdel, F., Rademacher, A., Vlijm, R., Tunnermann, J., Frank, L., Weinmann, R., Schweigert, E., Yserentant,  
903 K., Hummert, J., Bauer, C., *et al.* (2020). Mouse Heterochromatin Adopts Digital Compaction States  
904 without Showing Hallmarks of HP1-Driven Liquid-Liquid Phase Separation. *Mol Cell* **78**, 236-249 e237.  
905 Franzmann, T.M., and Alberti, S. (2019). Protein Phase Separation as a Stress Survival Strategy. *Cold*  
906 *Spring Harb Perspect Biol.*  
907 Franzmann, T.M., Jahnel, M., Pozniakovsky, A., Mahamid, J., Holehouse, A.S., Nuske, E., Richter, D.,  
908 Baumeister, W., Grill, S.W., Pappu, R.V., *et al.* (2018). Phase separation of a yeast prion protein  
909 promotes cellular fitness. *Science* **359**.  
910 Friedberg, E.C., Walker, G.C., Siede, W., Wood, R.D., Schultz, R.A., and Elenberger, T. (2006). DNA repair  
911 and mutagenesis, 2nd edn (Washington, D.C.: ASM Press).  
912 Garcia-Higuera, I., Taniguchi, T., Ganesan, S., Meyn, M.S., Timmers, C., Hejna, J., Grompe, M., and  
913 D'Andrea, A.D. (2001). Interaction of the Fanconi anemia proteins and BRCA1 in a common pathway.  
914 *Mol Cell* **7**, 249-262.  
915 Greer, D.A., Besley, B.D., Kennedy, K.B., and Davey, S. (2003). hRad9 rapidly binds DNA containing  
916 double-strand breaks and is required for damage-dependent topoisomerase II beta binding protein 1  
917 focus formation. *Cancer Res* **63**, 4829-4835.  
918 Haahr, P., Hoffmann, S., Tollenaere, M.A., Ho, T., Toledo, L.I., Mann, M., Bekker-Jensen, S., Raschle, M.,  
919 and Mailand, N. (2016). Activation of the ATR kinase by the RPA-binding protein ETAA1. *Nat Cell Biol* **18**,  
920 1196-1207.  
921 Hashimoto, Y., and Takisawa, H. (2003). Xenopus Cut5 is essential for a CDK-dependent process in the  
922 initiation of DNA replication. *EMBO J* **22**, 2526-2535.  
923 Hashimoto, Y., Tsujimura, T., Sugino, A., and Takisawa, H. (2006). The phosphorylated C-terminal domain  
924 of Xenopus Cut5 directly mediates ATR-dependent activation of Chk1. *Genes Cells* **11**, 993-1007.  
925 Hyman, A.A., and Simons, K. (2012). Cell biology. Beyond oil and water--phase transitions in cells.  
926 *Science* **337**, 1047-1049.  
927 Jackson, S.P., and Bartek, J. (2009). The DNA-damage response in human biology and disease. *Nature*  
928 **461**, 1071-1078.  
929 Kasahara, K., Goto, H., Enomoto, M., Tomono, Y., Kiyono, T., and Inagaki, M. (2010). 14-3-3gamma  
930 mediates Cdc25A proteolysis to block premature mitotic entry after DNA damage. *EMBO J* **29**, 2802-  
931 2812.  
932 Kilic, S., Lezaja, A., Gatti, M., Bianco, E., Michelena, J., Imhof, R., and Altmeyer, M. (2019). Phase  
933 separation of 53BP1 determines liquid-like behavior of DNA repair compartments. *The EMBO Journal*  
934 *e101379*.  
935 Kroschwald, S., Maharana, S., and Alberti, S. (2017). Hexanediol: a chemical probe to investigate the  
936 material properties of membrane-less compartments. *matters*, 1-7.  
937 Kumagai, A., Lee, J., Yoo, H.Y., and Dunphy, W.G. (2006). TopBP1 activates the ATR-ATRIP complex. *Cell*  
938 **124**, 943-955.  
939 Kwon, I., Kato, M., Xiang, S., Wu, L., Theodoropoulos, P., Mirzaei, H., Han, T., Xie, S., Corden, J.L., and  
940 McKnight, S.L. (2013). Phosphorylation-regulated binding of RNA polymerase II to fibrous polymers of  
941 low-complexity domains. *Cell* **155**, 1049-1060.  
942 Lee, Y.C., Zhou, Q., Chen, J., and Yuan, J. (2016). RPA-Binding Protein ETAA1 Is an ATR Activator Involved  
943 in DNA Replication Stress Response. *Curr Biol* **26**, 3257-3268.  
944 Leimbacher, P.A., Jones, S.E., Shorrocks, A.K., de Marco Zompit, M., Day, M., Blaauwendraad, J.,  
945 Bundschuh, D., Bonham, S., Fischer, R., Fink, D., *et al.* (2019). MDC1 Interacts with TOPBP1 to Maintain  
946 Chromosomal Stability during Mitosis. *Mol Cell*.  
947 Lin, S.J., Wardlaw, C.P., Morishita, T., Miyabe, I., Chahwan, C., Caspari, T., Schmidt, U., Carr, A.M., and  
948 Garcia, V. (2012). The Rad4(TopBP1) ATR-activation domain functions in G1/S phase in a chromatin-  
949 dependent manner. *PLoS Genet* **8**, e1002801.

950 Lindahl, T. (1993). Instability and decay of the primary structure of DNA. *Nature* 362, 709-715.

951 Lindsey-Boltz, L.A., and Sancar, A. (2011). Tethering DNA damage checkpoint mediator proteins

952 topoisomerase IIbeta-binding protein 1 (TopBP1) and Claspin to DNA activates ataxia-telangiectasia

953 mutated and RAD3-related (ATR) phosphorylation of checkpoint kinase 1 (Chk1). *J Biol Chem* 286,

954 19229-19236.

955 Lisby, M., Rothstein, R., and Mortensen, U.H. (2001). Rad52 forms DNA repair and recombination

956 centers during S phase. *Proc Natl Acad Sci U S A* 98, 8276-8282.

957 Liu, K., Bellam, N., Lin, H.Y., Wang, B., Stockard, C.R., Grizzle, W.E., and Lin, W.C. (2009). Regulation of

958 p53 by TopBP1: a potential mechanism for p53 inactivation in cancer. *Mol Cell Biol* 29, 2673-2693.

959 Liu, S., Bekker-Jensen, S., Mailand, N., Lukas, C., Bartek, J., and Lukas, J. (2006). Claspin operates

960 downstream of TopBP1 to direct ATR signaling towards Chk1 activation. *Mol Cell Biol* 26, 6056-6064.

961 Liu, Y., Cussiol, J.R., Dibitetto, D., Sims, J.R., Twayana, S., Weiss, R.S., Freire, R., Marini, F., Pelliccioli, A.,

962 and Smolka, M.B. (2017). TOPBP1(Dpb11) plays a conserved role in homologous recombination DNA

963 repair through the coordinated recruitment of 53BP1(Rad9). *J Cell Biol* 216, 623-639.

964 Lu, H., Yu, D., Hansen, A.S., Ganguly, S., Liu, R., Heckert, A., Darzacq, X., and Zhou, Q. (2018). Phase-

965 separation mechanism for C-terminal hyperphosphorylation of RNA polymerase II. *Nature* 558, 318-323.

966 Makiniemi, M., Hillukkala, T., Tuusa, J., Reini, K., Vaara, M., Huang, D., Pospiech, H., Majuri, I.,

967 Westerling, T., Makela, T.P., *et al.* (2001). BRCT domain-containing protein TopBP1 functions in DNA

968 replication and damage response. *J Biol Chem* 276, 30399-30406.

969 Mao, Y.S., Sunwoo, H., Zhang, B., and Spector, D.L. (2011). Direct visualization of the co-transcriptional

970 assembly of a nuclear body by noncoding RNAs. *Nat Cell Biol* 13, 95-101.

971 Marechal, A., and Zou, L. (2013). DNA damage sensing by the ATM and ATR kinases. *Cold Spring Harb*

972 *Perspect Biol* 5.

973 Maser, R.S., Monsen, K.J., Nelms, B.E., and Petrini, J.H. (1997). hMre11 and hRad50 nuclear foci are

974 induced during the normal cellular response to DNA double-strand breaks. *Mol Cell Biol* 17, 6087-6096.

975 McSwiggen, D.T., Hansen, A.S., Teves, S.S., Marie-Nelly, H., Hao, Y., Heckert, A.B., Umemoto, K.K.,

976 Dugast-Darzacq, C., Tjian, R., and Darzacq, X. (2019). Evidence for DNA-mediated nuclear

977 compartmentalization distinct from phase separation. *Elife* 8.

978 Michelena, J., Gatti, M., Teloni, F., Imhof, R., and Altmeyer, M. (2019). Basal CHK1 activity safeguards its

979 stability to maintain intrinsic S-phase checkpoint functions. *J Cell Biol* 218, 2865-2875.

980 Mordes, D.A., Glick, G.G., Zhao, R., and Cortez, D. (2008). TopBP1 activates ATR through ATRIP and a

981 PIKK regulatory domain. *Genes Dev* 22, 1478-1489.

982 Moudry, P., Watanabe, K., Wolanin, K.M., Bartkova, J., Wassing, I.E., Watanabe, S., Strauss, R.,

983 Troelsgaard Pedersen, R., Oestergaard, V.H., Lisby, M., *et al.* (2016). TOPBP1 regulates RAD51

984 phosphorylation and chromatin loading and determines PARP inhibitor sensitivity. *J Cell Biol* 212, 281-

985 288.

986 Munk, S., Sigurethsson, J.O., Xiao, Z., Batth, T.S., Franciosa, G., von Stechow, L., Lopez-Contreras, A.J.,

987 Vertegaal, A.C.O., and Olsen, J.V. (2017). Proteomics Reveals Global Regulation of Protein SUMOylation

988 by ATM and ATR Kinases during Replication Stress. *Cell Rep* 21, 546-558.

989 Park, M.S., Knauf, J.A., Pendergrass, S.H., Coulon, C.H., Strniste, G.F., Marrone, B.L., and MacInnes, M.A.

990 (1996). Ultraviolet-induced movement of the human DNA repair protein, Xeroderma pigmentosum type

991 G, in the nucleus. *Proc Natl Acad Sci U S A* 93, 8368-8373.

992 Patel, A., Lee, H.O., Jawerth, L., Maharana, S., Jahnel, M., Hein, M.Y., Stoyanov, S., Mahamid, J., Saha, S.,

993 Franzmann, T.M., *et al.* (2015). A Liquid-to-Solid Phase Transition of the ALS Protein FUS Accelerated by

994 Disease Mutation. *Cell* 162, 1066-1077.

995 Pedersen, R.T., Kruse, T., Nilsson, J., Oestergaard, V.H., and Lisby, M. (2015). TopBP1 is required at

996 mitosis to reduce transmission of DNA damage to G1 daughter cells. *J Cell Biol* 210, 565-582.

997 Pessina, F., Giavazzi, F., Yin, Y., Gioia, U., Vitelli, V., Galbiati, A., Barozzi, S., Garre, M., Oldani, A., Flaus,  
998 A., *et al.* (2019). Functional transcription promoters at DNA double-strand breaks mediate RNA-driven  
999 phase separation of damage-response factors. *Nat Cell Biol.*

1000 Prior, I.A., Muncke, C., Parton, R.G., and Hancock, J.F. (2003). Direct visualization of Ras proteins in  
1001 spatially distinct cell surface microdomains. *J Cell Biol* *160*, 165-170.

1002 Riback, J.A., Katanski, C.D., Kear-Scott, J.L., Pilipenko, E.V., Rojek, A.E., Sosnick, T.R., and Drummond,  
1003 D.A. (2017). Stress-Triggered Phase Separation Is an Adaptive, Evolutionarily Tuned Response. *Cell* *168*,  
1004 1028-1040 e1019.

1005 Sabari, B.R., Dall'Agnesse, A., Boija, A., Klein, I.A., Coffey, E.L., Shrinivas, K., Abraham, B.J., Hannett, N.M.,  
1006 Zamudio, A.V., Manteiga, J.C., *et al.* (2018). Coactivator condensation at super-enhancers links phase  
1007 separation and gene control. *Science* *361*.

1008 Saldivar, J.C., Cortez, D., and Cimprich, K.A. (2017). The essential kinase ATR: ensuring faithful  
1009 duplication of a challenging genome. *Nat Rev Mol Cell Biol* *18*, 622-636.

1010 Shin, Y., Berry, J., Pannucci, N., Haataja, M.P., Toettcher, J.E., and Brangwynne, C.P. (2017).  
1011 Spatiotemporal Control of Intracellular Phase Transitions Using Light-Activated optoDroplets. *Cell* *168*,  
1012 159-171 e114.

1013 Shin, Y., and Brangwynne, C.P. (2017). Liquid phase condensation in cell physiology and disease. *Science*  
1014 *357*.

1015 Shin, Y., Chang, Y.C., Lee, D.S.W., Berry, J., Sanders, D.W., Ronceray, P., Wingreen, N.S., Haataja, M., and  
1016 Brangwynne, C.P. (2018). Liquid Nuclear Condensates Mechanically Sense and Restructure the Genome.  
1017 *Cell* *175*, 1481-1491 e1413.

1018 Soding, J., Zwicker, D., Sohrabi-Jahromi, S., Boehning, M., and Kirschbaum, J. (2020). Mechanisms for  
1019 Active Regulation of Biomolecular Condensates. *Trends Cell Biol* *30*, 4-14.

1020 Sokka, M., Rilla, K., Miinalainen, I., Pospiech, H., and Syvaoja, J.E. (2015). High levels of TopBP1 induce  
1021 ATR-dependent shut-down of rRNA transcription and nucleolar segregation. *Nucleic Acids Res* *43*, 4975-  
1022 4989.

1023 Thada, V., and Cortez, D. (2019). Common motifs in ETAA1 and TOPBP1 required for ATR kinase  
1024 activation. *J Biol Chem* *294*, 8395-8402.

1025 Tian, T., Harding, A., Inder, K., Plowman, S., Parton, R.G., and Hancock, J.F. (2007). Plasma membrane  
1026 nanoswitches generate high-fidelity Ras signal transduction. *Nat Cell Biol* *9*, 905-914.

1027 Tubbs, A., and Nussenzweig, A. (2017). Endogenous DNA Damage as a Source of Genomic Instability in  
1028 Cancer. *Cell* *168*, 644-656.

1029 Van, C., Yan, S., Michael, W.M., Waga, S., and Cimprich, K.A. (2010). Continued primer synthesis at  
1030 stalled replication forks contributes to checkpoint activation. *J Cell Biol* *189*, 233-246.

1031 Vidal-Eychenie, S., Decaillet, C., Basbous, J., and Constantinou, A. (2013). DNA structure-specific priming  
1032 of ATR activation by DNA-PKcs. *J Cell Biol* *202*, 421-429.

1033 Wang, X., Ran, T., Zhang, X., Xin, J., Zhang, Z., Wu, T., Wang, W., and Cai, G. (2017). 3.9 Å structure of the  
1034 yeast Mec1-Ddc2 complex, a homolog of human ATR-ATRIP. *Science* *358*, 1206-1209.

1035 Woodruff, J.B., Ferreira Gomes, B., Widlund, P.O., Mahamid, J., Honigsmann, A., and Hyman, A.A. (2017).  
1036 The Centrosome Is a Selective Condensate that Nucleates Microtubules by Concentrating Tubulin. *Cell*  
1037 *169*, 1066-1077 e1010.

1038 Wright, R.H., Dornan, E.S., Donaldson, M.M., and Morgan, I.M. (2006). TopBP1 contains a transcriptional  
1039 activation domain suppressed by two adjacent BRCT domains. *Biochem J* *400*, 573-582.

1040 Yan, S., and Michael, W.M. (2009). TopBP1 and DNA polymerase alpha-mediated recruitment of the 9-1-  
1041 1 complex to stalled replication forks: implications for a replication restart-based mechanism for ATR  
1042 checkpoint activation. *Cell Cycle* *8*, 2877-2884.

1043 Yoo, H.Y., Kumagai, A., Shevchenko, A., and Dunphy, W.G. (2009). The Mre11-Rad50-Nbs1 complex  
1044 mediates activation of TopBP1 by ATM. *Mol Biol Cell* *20*, 2351-2360.

1045 Zhang, P., Fan, B., Yang, P., Temirov, J., Messing, J., Kim, H.J., and Taylor, J.P. (2019). Chronic optogenetic  
1046 induction of stress granules is cytotoxic and reveals the evolution of ALS-FTD pathology. *Elife* 8.  
1047 Zhou, Z.W., Liu, C., Li, T.L., Bruhn, C., Krueger, A., Min, W., Wang, Z.Q., and Carr, A.M. (2013). An  
1048 essential function for the ATR-activation-domain (AAD) of TopBP1 in mouse development and cellular  
1049 senescence. *PLoS Genet* 9, e1003702.  
1050 Zou, L., and Elledge, S.J. (2003). Sensing DNA damage through ATRIP recognition of RPA-ssDNA  
1051 complexes. *Science* 300, 1542-1548.

1052

## KEY RESOURCES TABLE

REAGENT or RESOURCE	SOURCE	IDENTIFIER
Antibodies		
ATR	Bethyl/euromedex	Cat# A300-137A; RRID:AB_185544
BRCA1 (C-20)	Santa Cruz Biotechnology	Cat# sc-642; RRID:AB_630944
Chk1	Santa Cruz Biotechnology	Cat# sc-8408; RRID:AB_627257
FANCJ/BRIP1	Novus Biologicals	Cat# NB100-416; RRID:AB_2066307
Flag-M2	Sigma-Aldrich	Cat# F1804; RRID:AB_262044
mCherry	Elabscience	Cat# E-AB-20087
MRE11	Novus Biologicals	Cat# NB100-142; RRID:AB_10077796
NOL11	Sigma-Aldrich	Cat# HPA022010; RRID:AB_2267158
pATR (T1989)	GeneTex	Cat# GTX128145; RRID:AB_2687562
pChk1 (Ser296)	Cell Signaling Technology	Cat# 2349; RRID:AB_2080323
pChk1 (Ser345)	Cell Signaling Technology	Cat# 2348; RRID:AB_331212
pTopBP1 (Ser1138)	Interchim	Cat# orb140434
Streptavidin, Alexa Fluor 488 conjugate	Molecular Probes	Cat# S32354; RRID:AB_2315383
Tubulin (B-5-1-2)	Sigma-Aldrich	Cat# T5168; RRID:AB_477579
TopBP1	Bethyl	Cat# A300-111A; RRID:AB_2272050
Alexa Fluor 546 goat anti-mouse IgG	Molecular Probes	Cat# A-11030; RRID:AB_144695
Alexa Fluor 546 goat anti-rabbit IgG	Molecular Probes	Cat# A-11010; RRID:AB_2534077
Alexa Fluor 488 goat anti-mouse IgG2b	Molecular Probes	Cat# A-21141; RRID:AB_141626
Alexa Fluor 488 goat anti-rabbit IgG	Molecular Probes	Cat# A-21141; RRID:AB_141626
Anti-rabbit IgG Atto-647N	Sigma-Aldrich	Cat# 40839; RRID:AB_1137669
Anti-mouse IgG Atto-647N	Sigma-Aldrich	Cat# 50185; RRID:AB_1137661
Anti-mouse IgG Abberior STAR 580	Sigma-Aldrich	Cat# 38377
Anti-mouse IgG, HRP linked Antibody	Cell Signaling Technology	Cat# 7076; RRID:AB_330924
Anti-rabbit IgG, HRP linked Antibody	Cell Signaling Technology	Cat# 7074; RRID:AB_2099233
Bacterial and Virus Strains		
5-alpha Competent <i>E. coli</i> (High Efficiency)	NEB	Cat# C2987
MAX Efficiency™ DH10Bac Competent Cells	ThermoFisher Scientific	Cat# 10361012
Chemicals, Peptides, and Recombinant Proteins		
Biotin	Sigma-Aldrich	Cat# B4501; CAS: 58-85-5
Doxycycline	Clontech	Cat# 631311; CAS: 10592-13-9
Blasticidin	InvivoGen	Cat# ant-bl
Hygromycin	Sigma-Aldrich	Cat# H3274; CAS: 31282-04-9.
Zeocin	ThermoFisher Scientific	Cat# R25001

Ampicilin	Sigma-Aldrich	Cat# A9518; CAS: 69-52-3
Penicillin streptomycin	Sigma-Aldrich	Cat# P0781; ID 329820056
Gentamicin Sulfate	Sigma-Aldrich	Cat# G1914; CAS: 1405-41-0
X-Gal	Merck	Cat# 10745740001; CAS: 7240-90-6
IPTG	Sigma-Aldrich	Cat# I6758; CAS: 367-93-1
cOmplete, EDTA free	Roche	Cat# 4693159001
Halt phosphatase inhibitor cocktail	ThermoFisher Scientific	Cat# 78427
Benzonase Nuclease	Sigma-Aldrich	Cat# E1014; CAS: 9025-65-4
Ethidium bromide solution	Sigma-Aldrich	Cat# E1510; CAS: 1239-45-8
Adenosine 5'-triphosphate disodium salt hydrate	Sigma-Aldrich	Cat# A7699; CAS:34369-07-8
Creatine kinase	Sigma-Aldrich	Cat# C9858; MDL: MFCD00151687
Phosphocreatine di(tris) salt	Sigma-Aldrich	Cat# P1937; CAS: 108321-17-1
5-Iodo-2'-deoxyuridine	Sigma-Aldrich	Cat# I7125; CAS: 54-42-2
5-Chloro-2'-deoxyuridine	Sigma-Aldrich	Cat# C6891; CAS: 50-90-8
ATR Inhibitor III, ETP-46464	Merck	Cat# 5005080001; CAS: 1345675-02-7
VE-821	TINIB-TOOLS	Cat# V134; CAS: 1232410-49-9
UCN-01	Sigma-Aldrich	Cat# U6508; CAS: 112953-11-4
Streptavidin-Agarose	Sigma-Aldrich	Cat# S1638; MDL: MCFD00082035
Dulbecco's Modified Eagle's Medium - high glucose	Sigma-Aldrich	Cat# D5796
McCoy's 5A Medium	Sigma-Aldrich	Cat# M9309; MDL: MFCD00217560
EX-CELL <sup>®</sup> 420 Serum-Free Medium for Insect Cells	Sigma-Aldrich	Cat# 14420c; MDL: MFCD01634638
BioWest - Fetal Bovine Serum	Eurobio Scientific	Cat# S1810
Critical Commercial Assays		
Quick Start <sup>™</sup> Bradford 1x Dye Reagent	Bio-Rad	Cat# 500-0205
Clarity western ECL substrate	Bio-Rad	Cat# 170-5061

Clarity max western ECL substrate	Bio-Rad	Cat# 1705062
Criterion TGX stain free gel 7,5%	Bio-Rad	Cat# 5678024
Criterion TGX stain free gel 4-15%	Bio-Rad	Cat# 5678084
Criterion TGX stain free gel 10%	Bio-Rad	Cat# 5671034
Mini-PROTEAN TGX Stain Free Gels, 7.5%	Bio-Rad	Cat# 4568023
Mini-PROTEAN TGX Stain Free Gels, 4-15%	Bio-Rad	Cat# 4568083
Mini-PROTEAN TGX Stain Free Gels, 10%	Bio-Rad	Cat# 4568033
Trans-Blot Turbo Transfer Pack 0,2µm Nitrocellulose Midi, 10 pack	Bio-Rad	Cat# 1704159
Trans-Blot Turbo Transfer Pack 0,2µm Nitrocellulose Mini, 10 pack	Bio-Rad	Cat# 1704158
Color Prestained Protein Standard, Broad Range	BioLABs	Cat# P7712S
HisTrap HP column	GE Healthcare	Cat# 71-5027-68 AF
HiTrap™ Desalting column	GE Healthcare	Cat# 71-7154-00 AM
HiPrep 26/10	GE Healthcare	Cat# 28-4026-52 AB
Cellfectin	ThermoFisher Scientific	Cat# P/N 58760
Lipofectamine 2000	ThermoFisher Scientific	Cat# 11668-019
SnakeSkin Dialysis Tubing	Thermo Fisher Scientific	Cat# 68700
Precision 3C	GenScript	Cat# Z03092-500
Deposited Data		
Raw and analyzed data	This paper	<a href="http://dx.doi.org/10.17632/6nf7b7ffb7.1">http://dx.doi.org/10.17632/6nf7b7ffb7.1</a>
Experimental Models: Cell Lines		
Flp-In™ T-REx™ 293	Invitrogen	Cat# R78007; RRID:CVCL_U427
RPE1 HTRT	Gift from Dr. Krzysztof Rogowski	N/A
U2OS	Gift from Dr. Mikko Sokka	N/A
Hela S3	ATCC	Cat# CCL-2.2; RRID:CVCL_0058
Sf9 Insect Cells - Novagen	Sigma-Aldrich	Cat# 71104-M
Oligonucleotides		
See Table S1 for the full list of oligonucleotides used in this study	This paper	N/A
Recombinant DNA		
pOG44 Flp-Recombinase Expression Vector	ThermoFisher Scientific	Cat# V600520
3xHA-TurboID-NLS_pCDNA3	Addgene	DOI: 10.1038/nbt.4201
pCDNA5_FRT-TO_Flag-BirA*	Gift from Dr. Brian Raught	N/A

pHR-mCherry-Cry2	Gift from Dr. Clifford Brangwynne	N/A
pCDNA5_FRT-TO_GFP-ETAA1	Gift from Dr. Niels Mailand	N/A
pDONR223-RAD9A	Montpellier Genomic Collection (MGC)	N/A
pCDNA5_FRT-TO_TurboID-mCherry-Cry2 (opto-module)	This paper	N/A
pCDNA5_FRT-TO_TurboID-TopBP1WT-mCherry-Cry2	This paper	N/A
pCDNA5_FRT-TO_TurboID-TopBP1W1145R-mCherry-Cry2	This paper	N/A
pCDNA5_FRT-TO_TurboID-ETAA1-mCherry-Cry2	This paper	N/A
pCDNA5_FRT-TO_TurboID-TopBP1 <sup>ETAA1</sup> -AAD-mCherry-Cry2	This paper	N/A
pCDNA5_FRT-TO_TurboID-RAD9A-mCherry-Cry2	This paper	N/A
pFastBac1_6His_MBP_TopBP1WT <sup>b6-8</sup> -mGFP	This paper	N/A
pFastBac1_6His_MBP_TopBP1W1145R <sup>b6-8</sup> -mGFP	This paper	N/A
pFastBac1_6His_MBP_TopBP1WT <sup>b6-8</sup> -mRFP	This paper	N/A
pFastBac1_6His_MBP_TopBP1W1145R <sup>b6-8</sup> -mRFP	This paper	N/A
pCDNA5_FRT-TO_Flag-BirA*-TopBP1WT	This paper	N/A
pCDNA5_FRT-TO_Flag-BirA*-TopBP1W1145R	This paper	N/A
pCDNA5_FRT-TO_mCherry-Cry2 (opto-module#)	This paper	N/A
pCDNA5_FRT-TO_TopBP1WT <sup>b6-8</sup> -mCherry-Cry2	This paper	N/A
pCDNA5_FRT-TO_TopBP1W1145R <sup>b6-8</sup> -mCherry-Cry2	This paper	N/A
pCDNA5_FRT-TO_AAD-NLS <sup>TopBP1</sup> -mCherry-Cry2	This paper	N/A
pCDNA5_FRT-TO_TurboID-TopBP1F1071A-mCherry-Cry2	This paper	N/A
pCDNA5_FRT-TO_TurboID-TopBP1S1138A-mCherry-Cry2	This paper	N/A
pCDNA5_FRT-TO_TurboID-TopBP1S1138D-mCherry-Cry2	This paper	N/A
Software and Algorithms		

Image Lab™ Software (Version 5.2.1)	Bio-Rad	<a href="http://www.bio-rad.com/fr-fr/product/image-lab-software?ID=KRE6P5E8Z">http://www.bio-rad.com/fr-fr/product/image-lab-software?ID=KRE6P5E8Z</a>
Cell Profiler 2.2.0	Cell image analysis software	DOI:10.1093/bioinformatics/btr095
Prism 8 (Version 8.4.2)	Graphpad Software	<a href="https://www.graphpad.com/scientific-software/prism/">https://www.graphpad.com/scientific-software/prism/</a>
Omero	OME Remote Objects software	DOI:10.1038/nmeth.1896.
MaxQuant (Version 1.5.5.1)	MaxQuant software	<a href="https://pubmed.ncbi.nlm.nih.gov/19029910/">https://pubmed.ncbi.nlm.nih.gov/19029910/</a>
IMARIS	Bitplane	<a href="https://imaris.oxinst.com">https://imaris.oxinst.com</a>
FIJI	Open source	<a href="https://imagej.net/Fiji">https://imagej.net/Fiji</a>

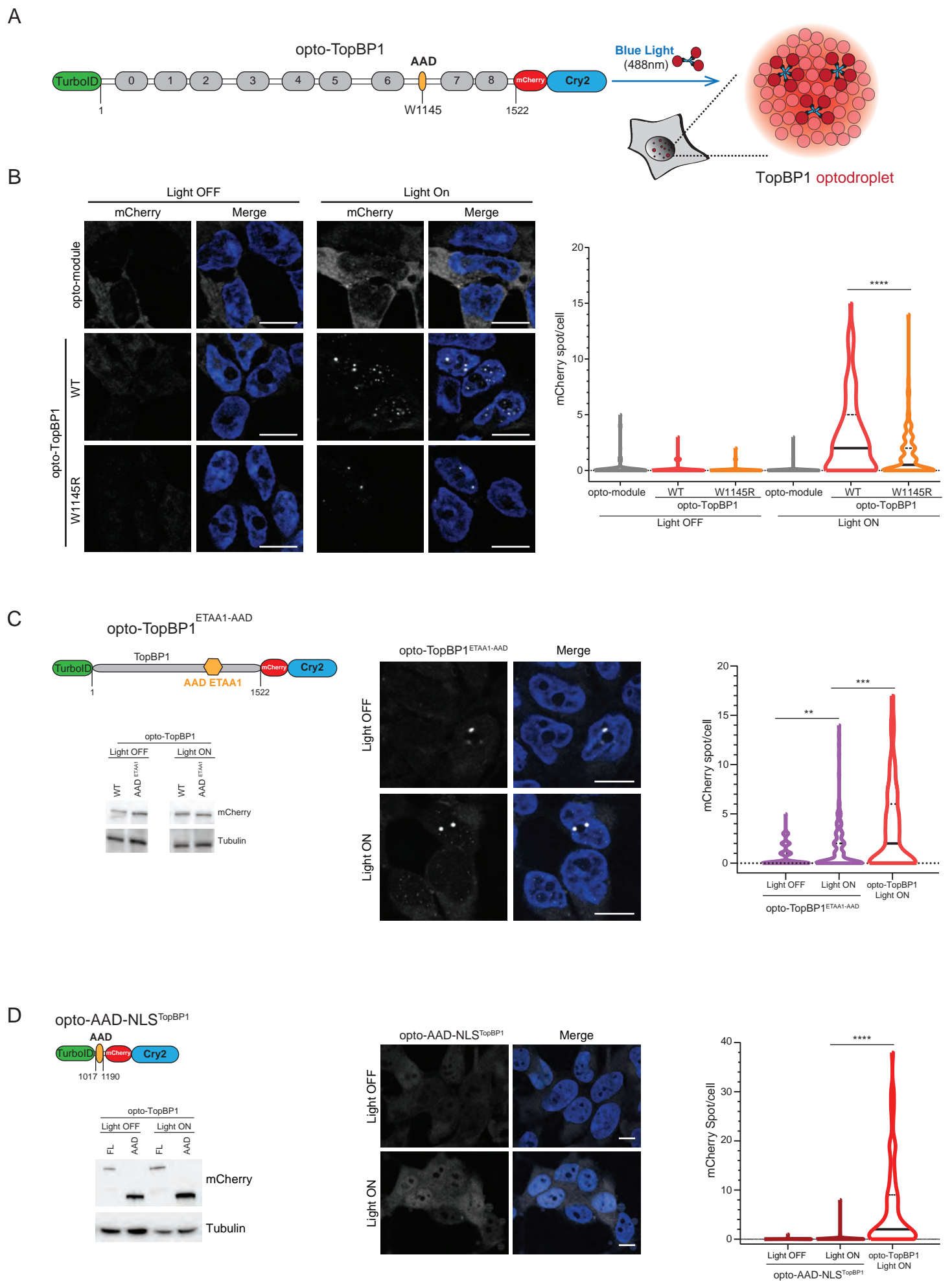


Figure 1

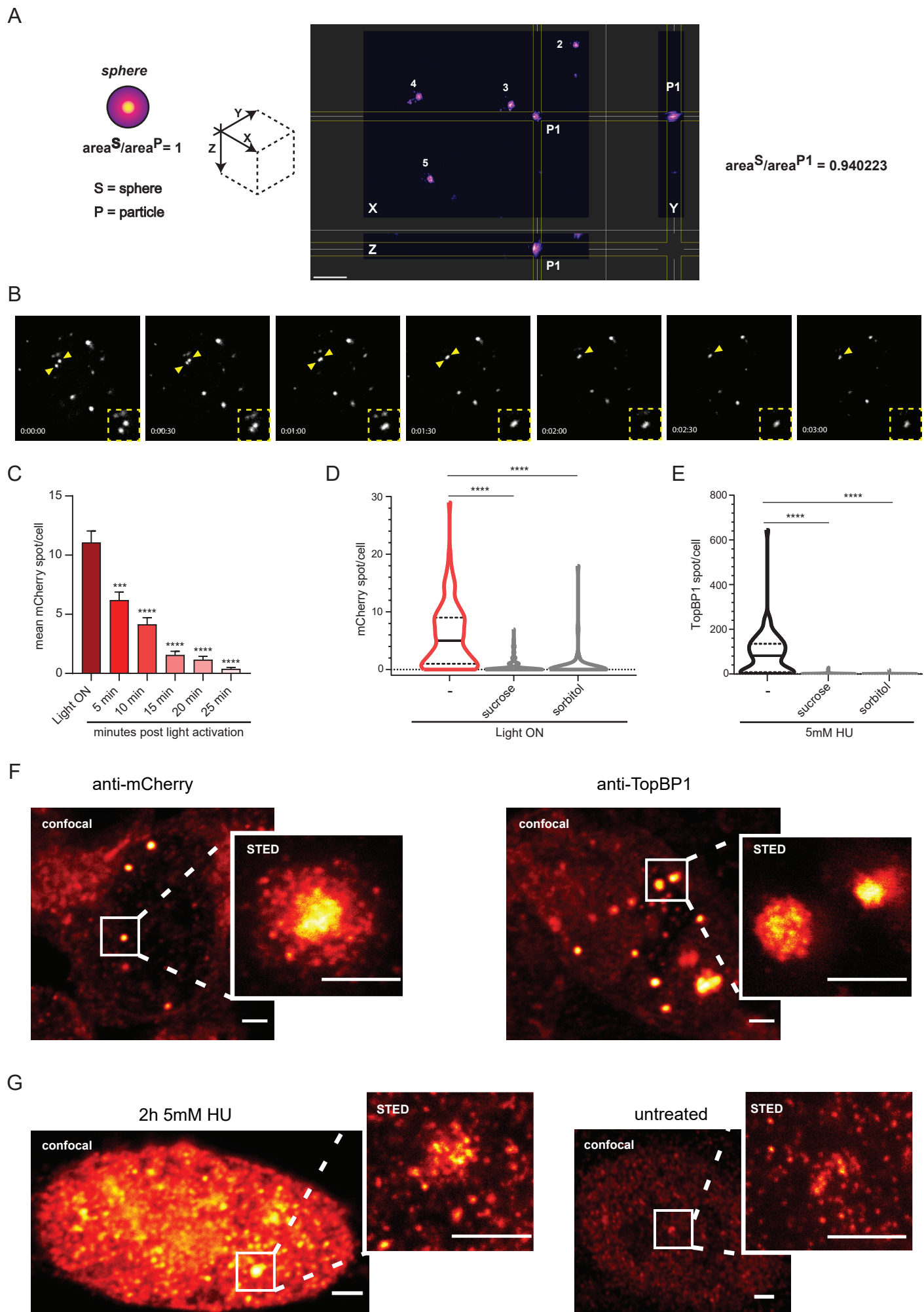


Figure 2

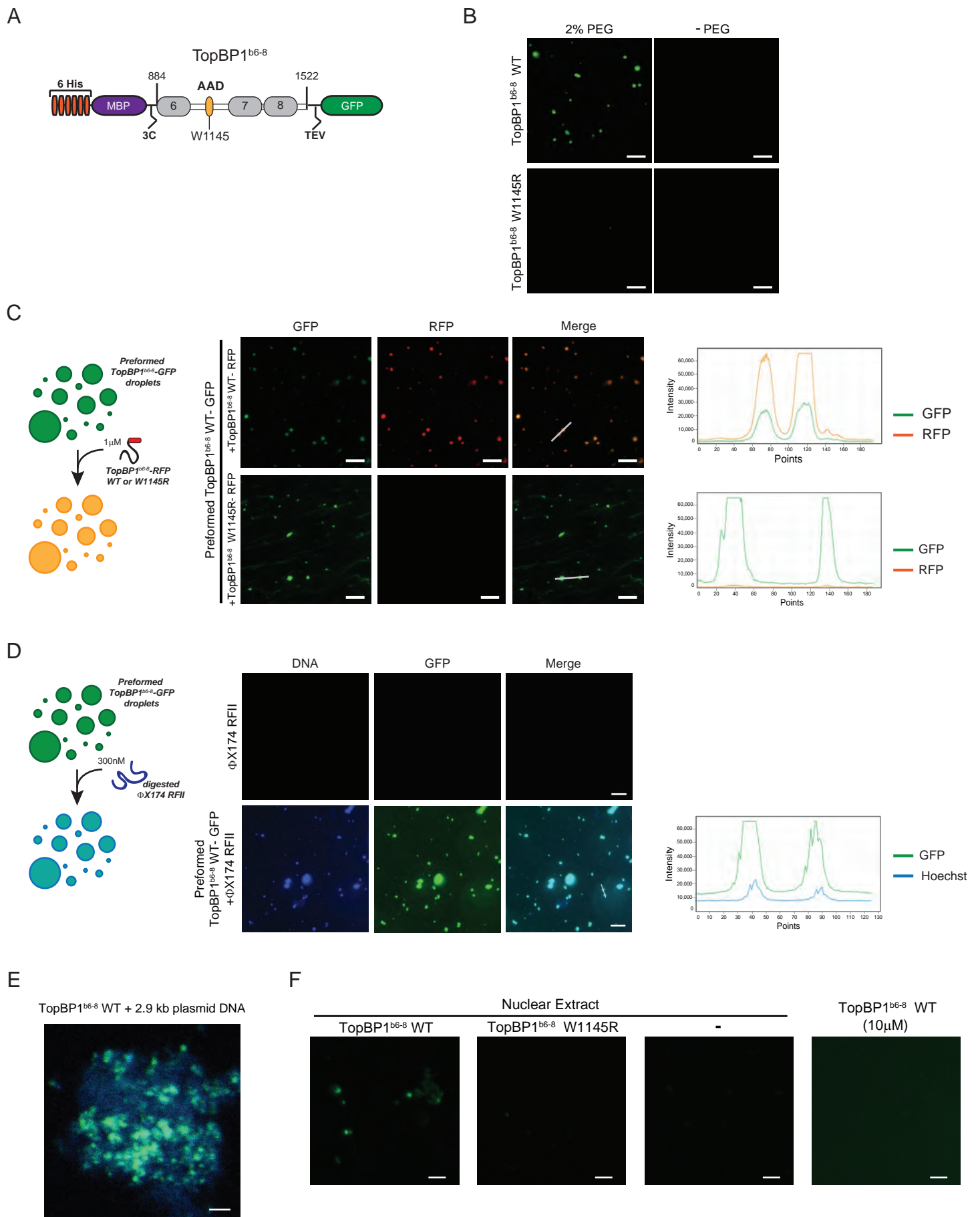


Figure 3

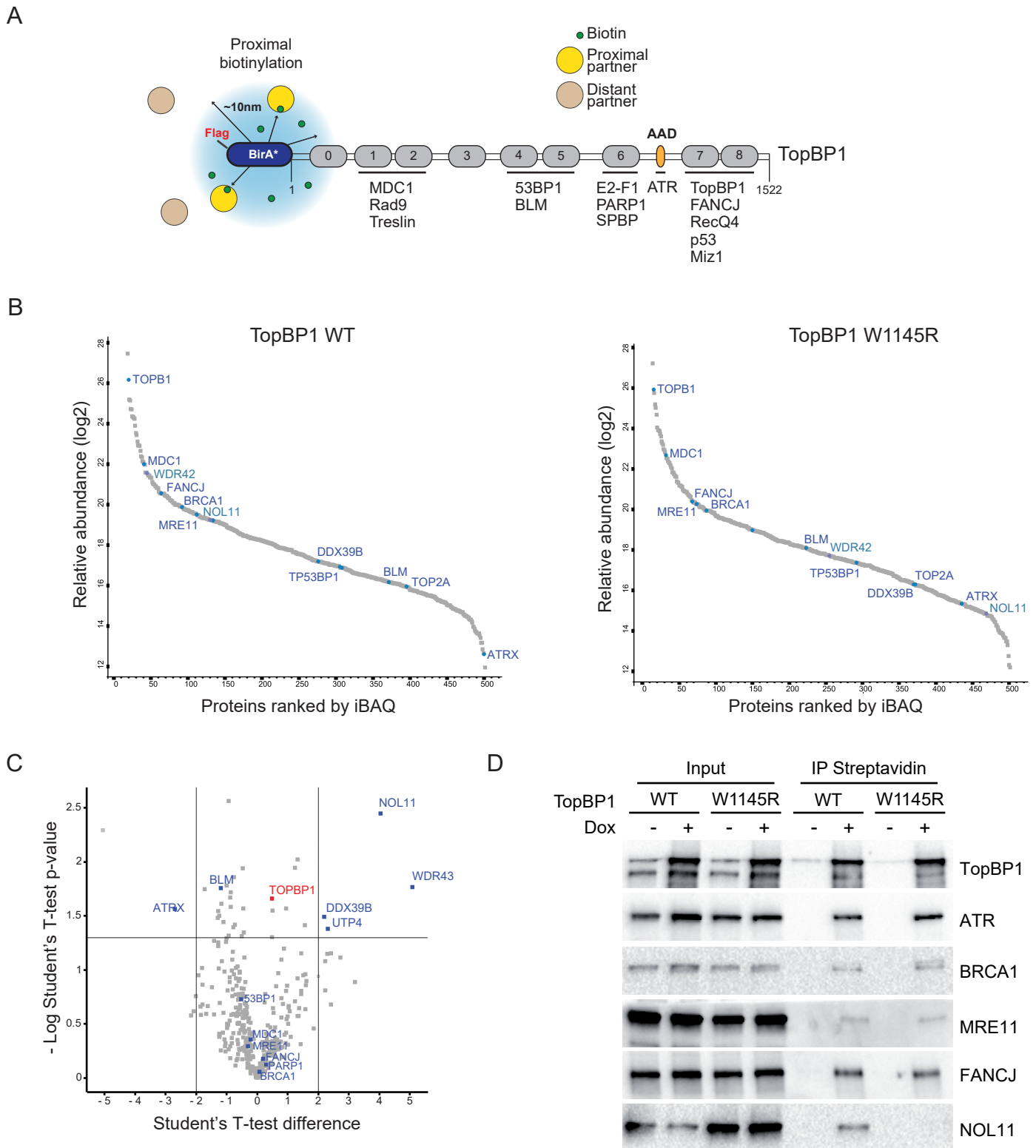


Figure 4

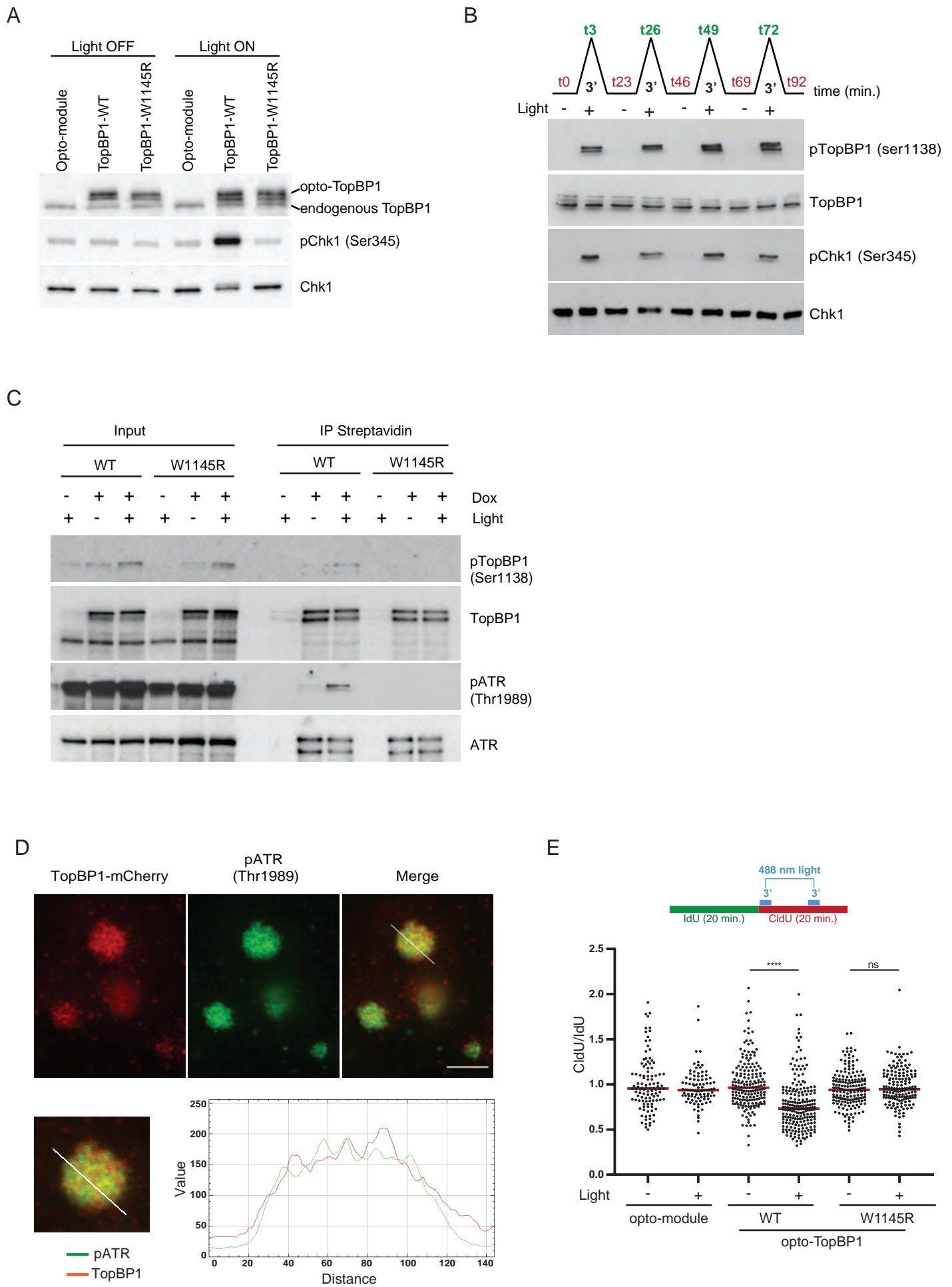


Figure 5

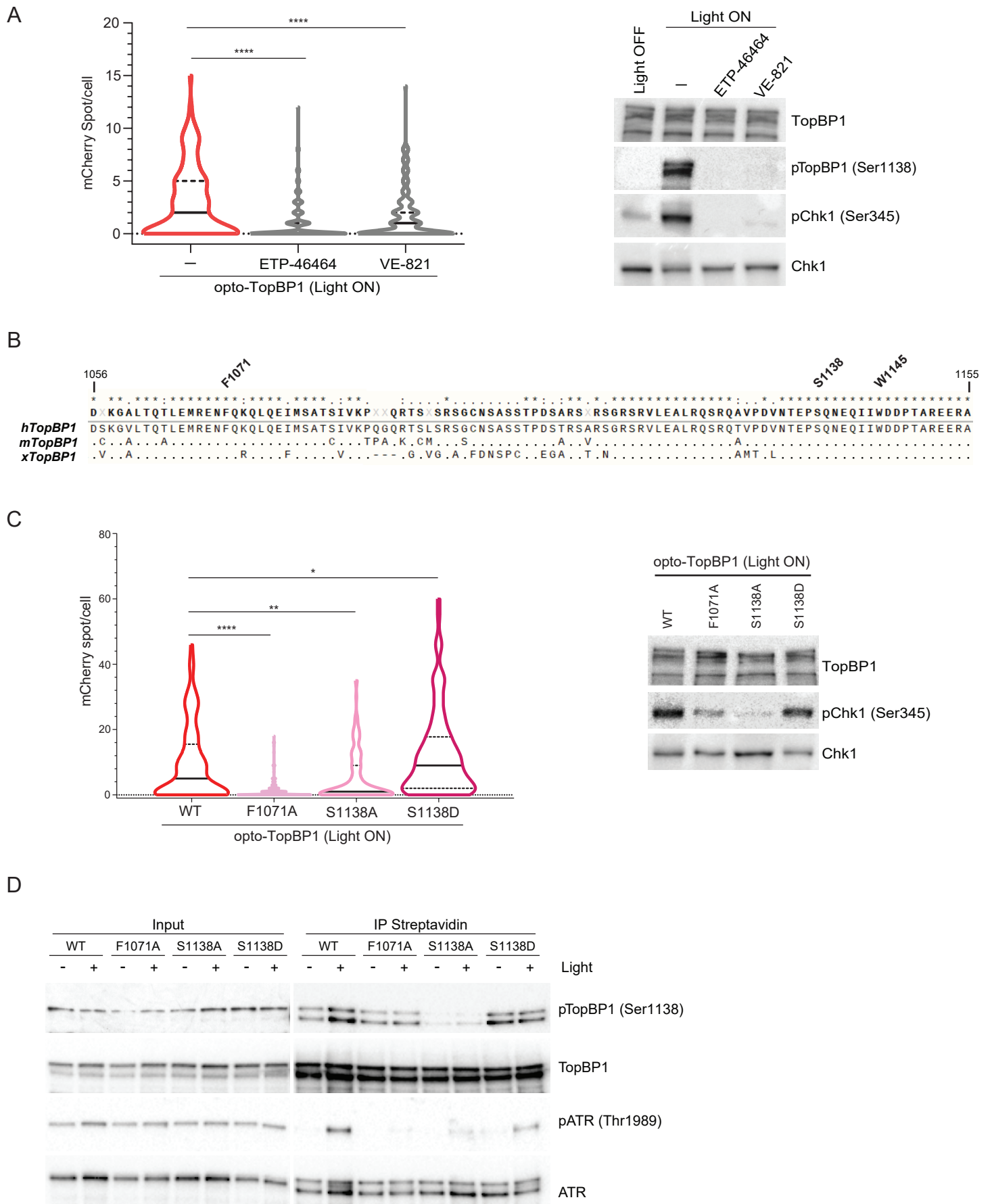
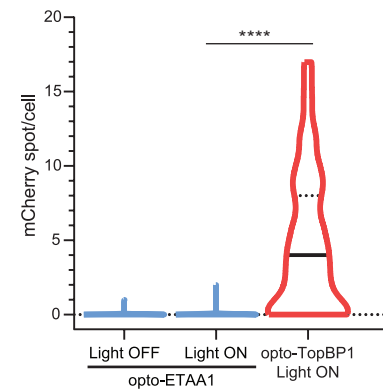
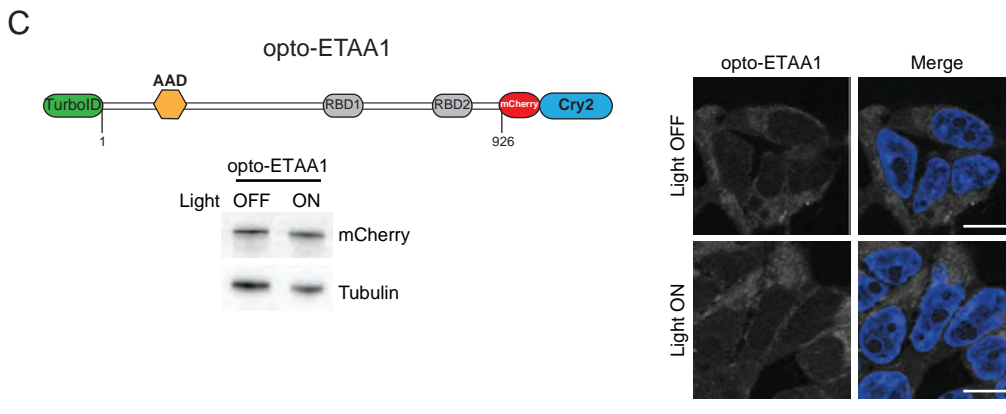
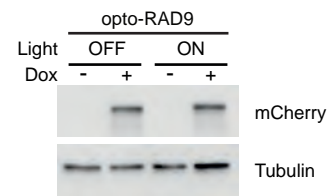
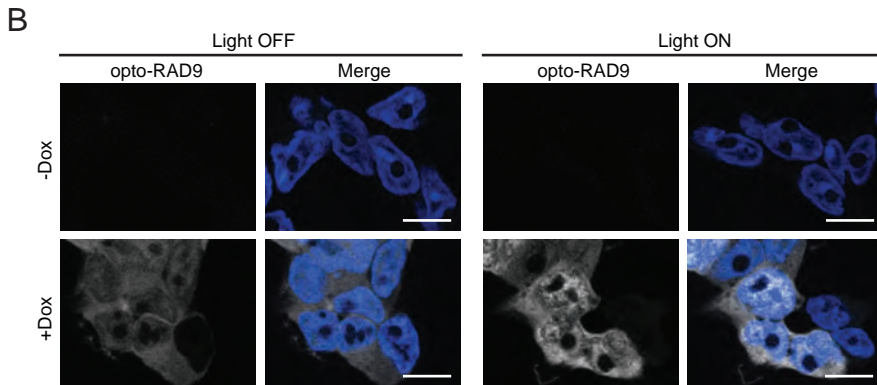
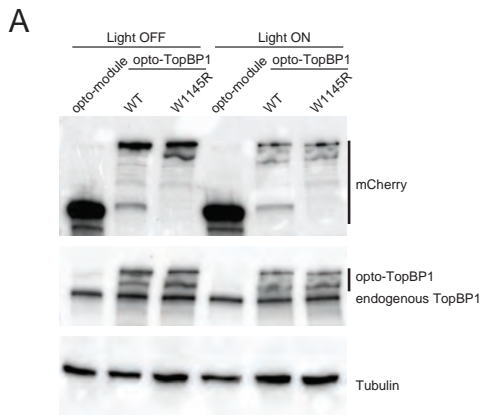
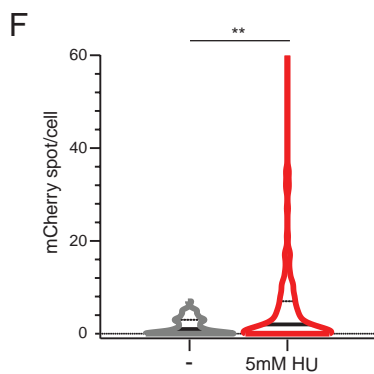
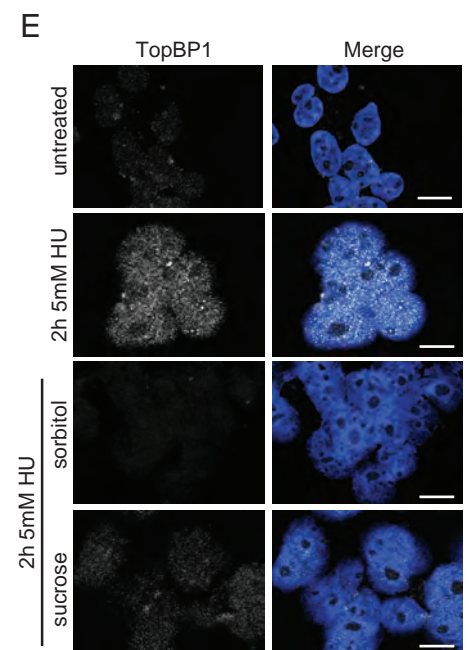
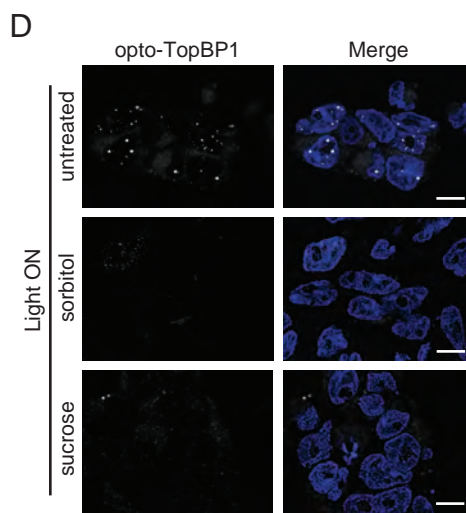
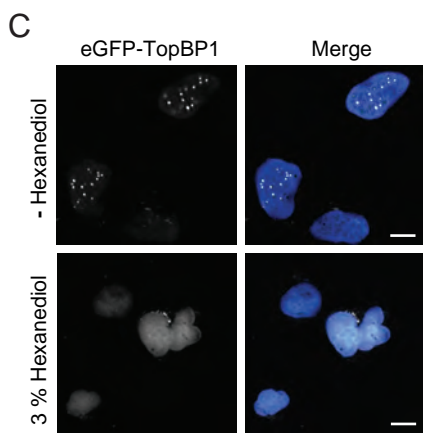
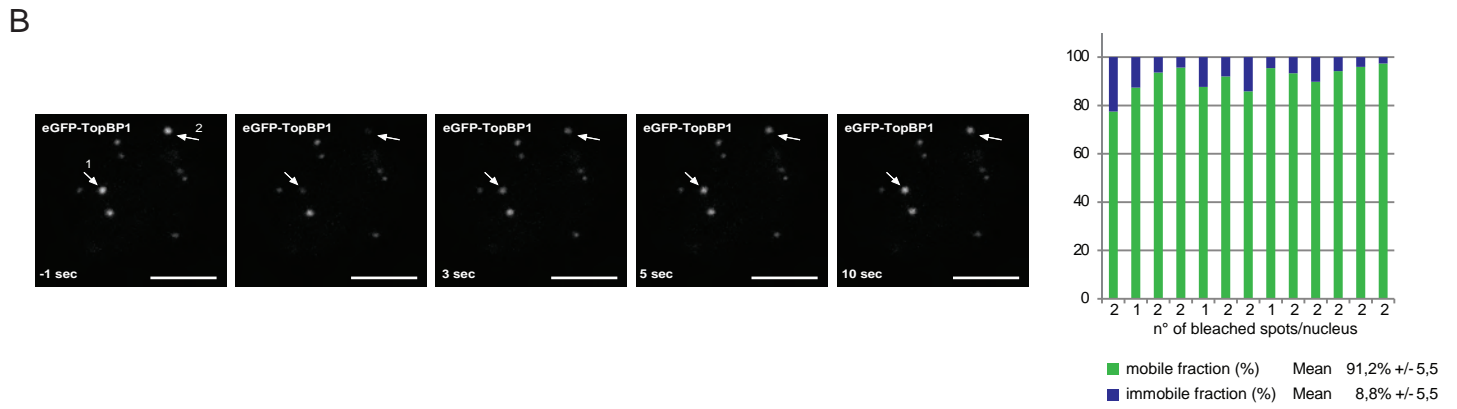
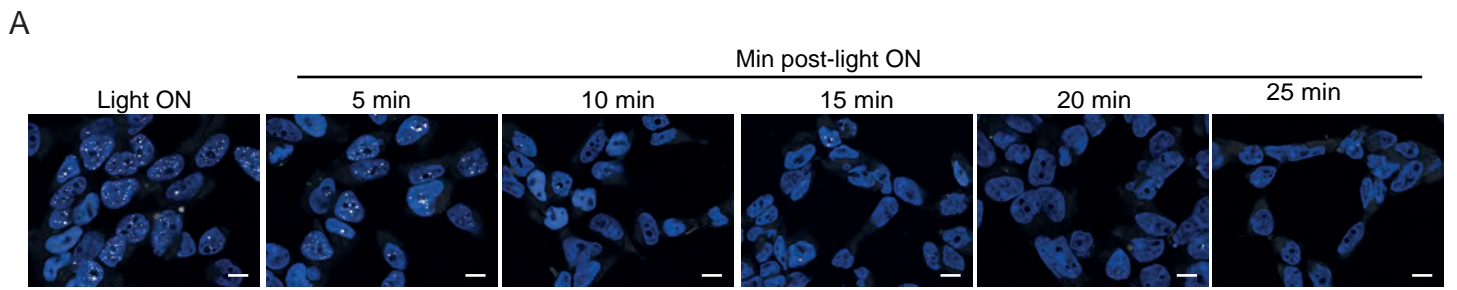
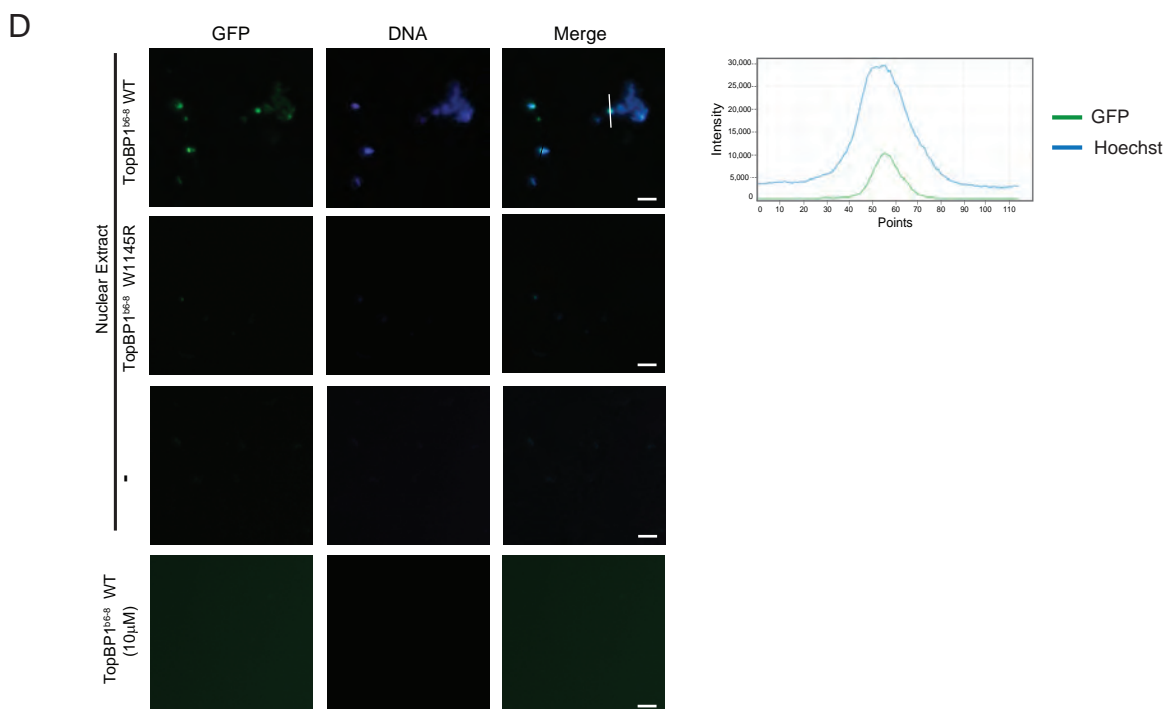
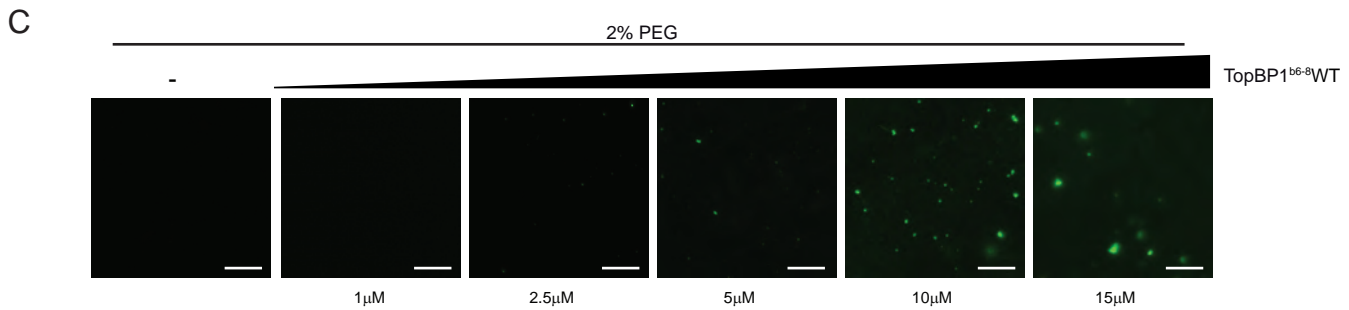
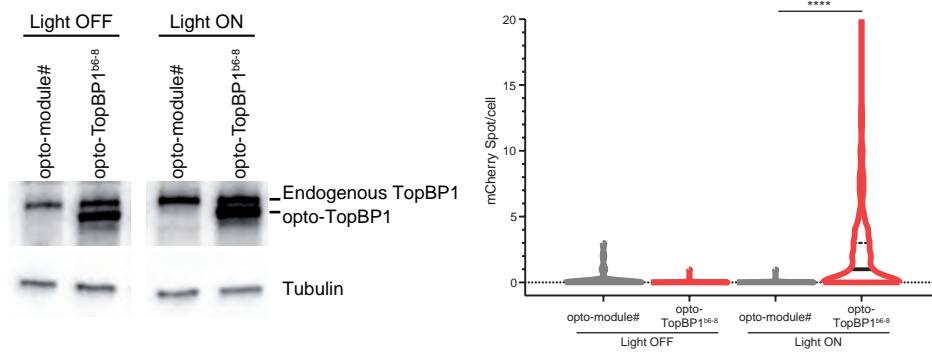
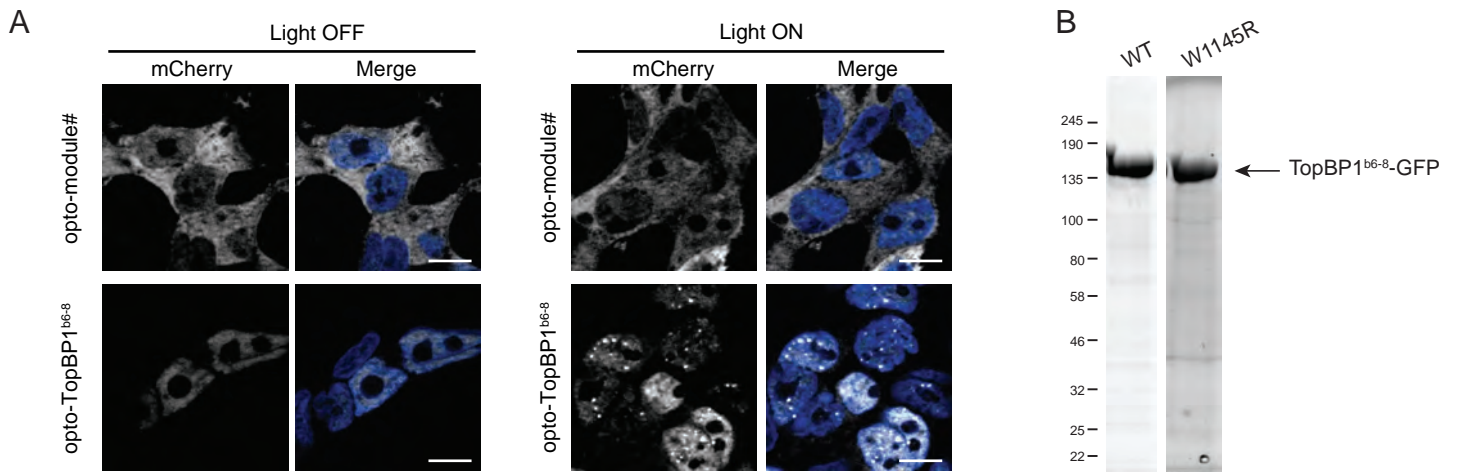


Figure 6

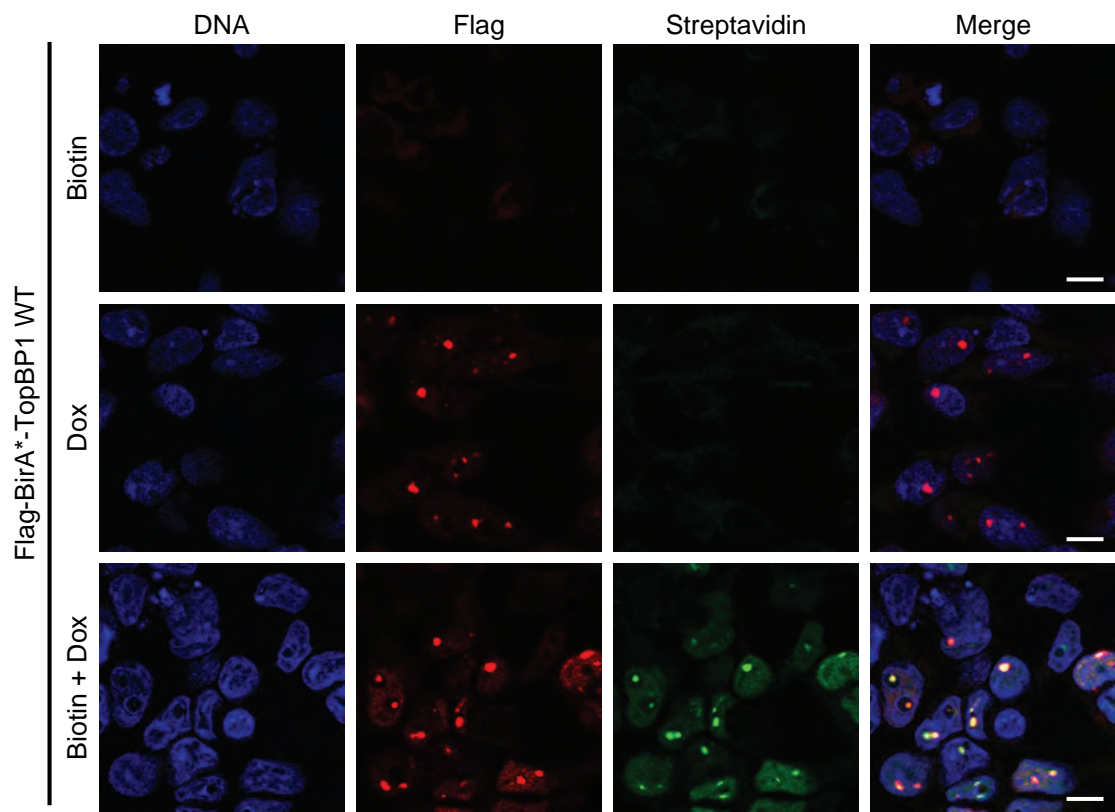




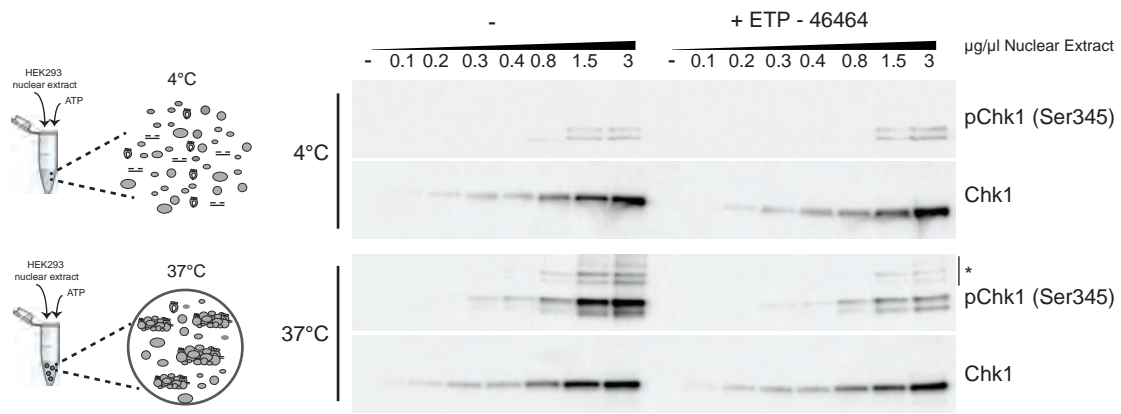




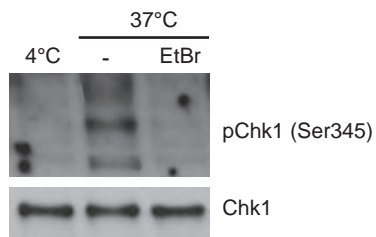
Suppl Figure 3\_related to Figure 3

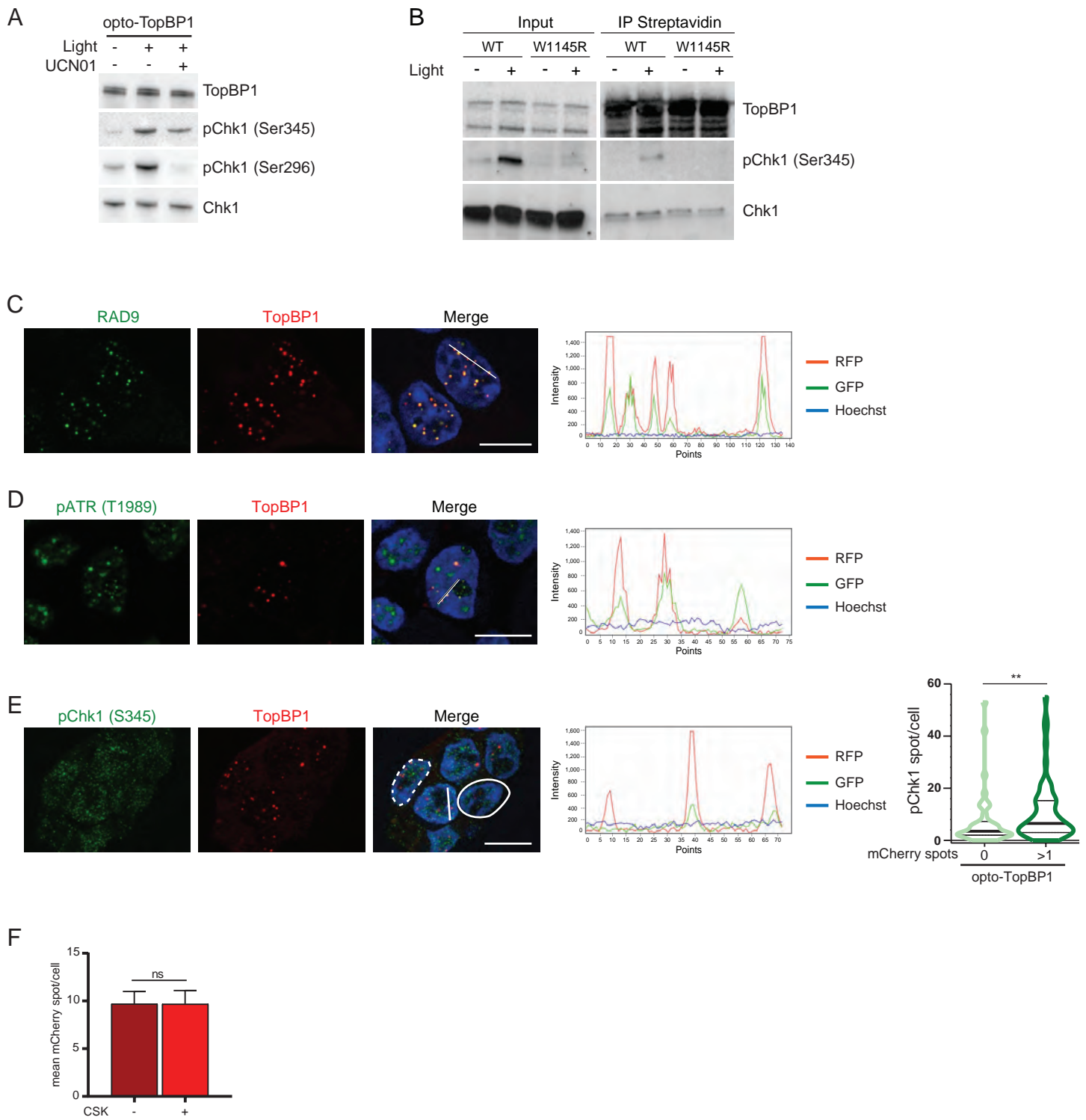


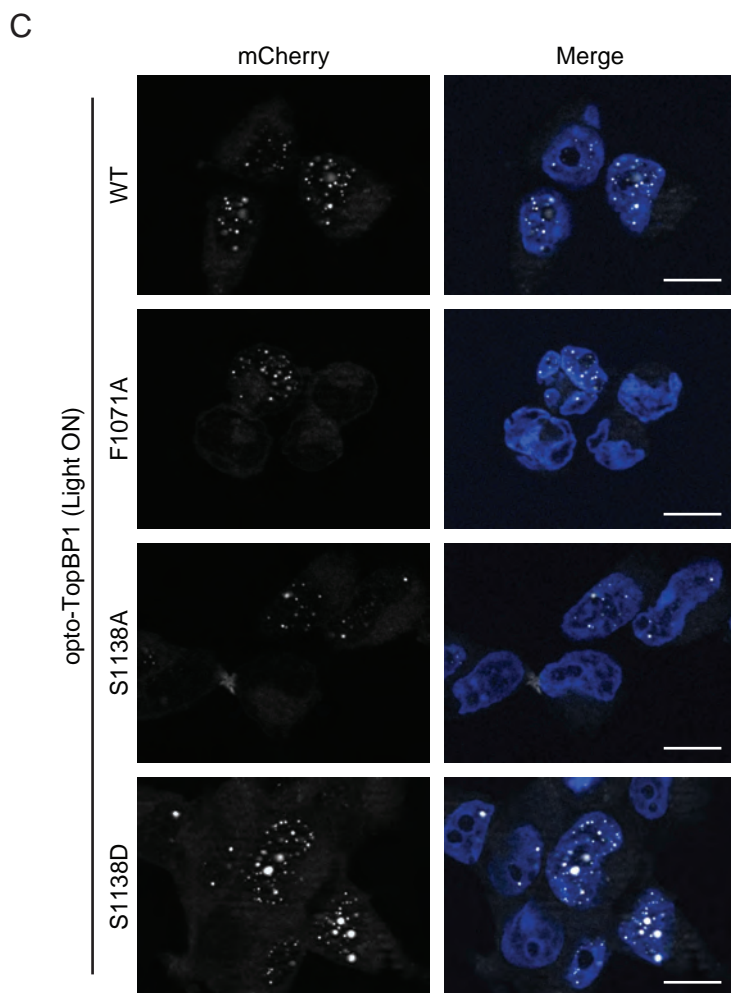
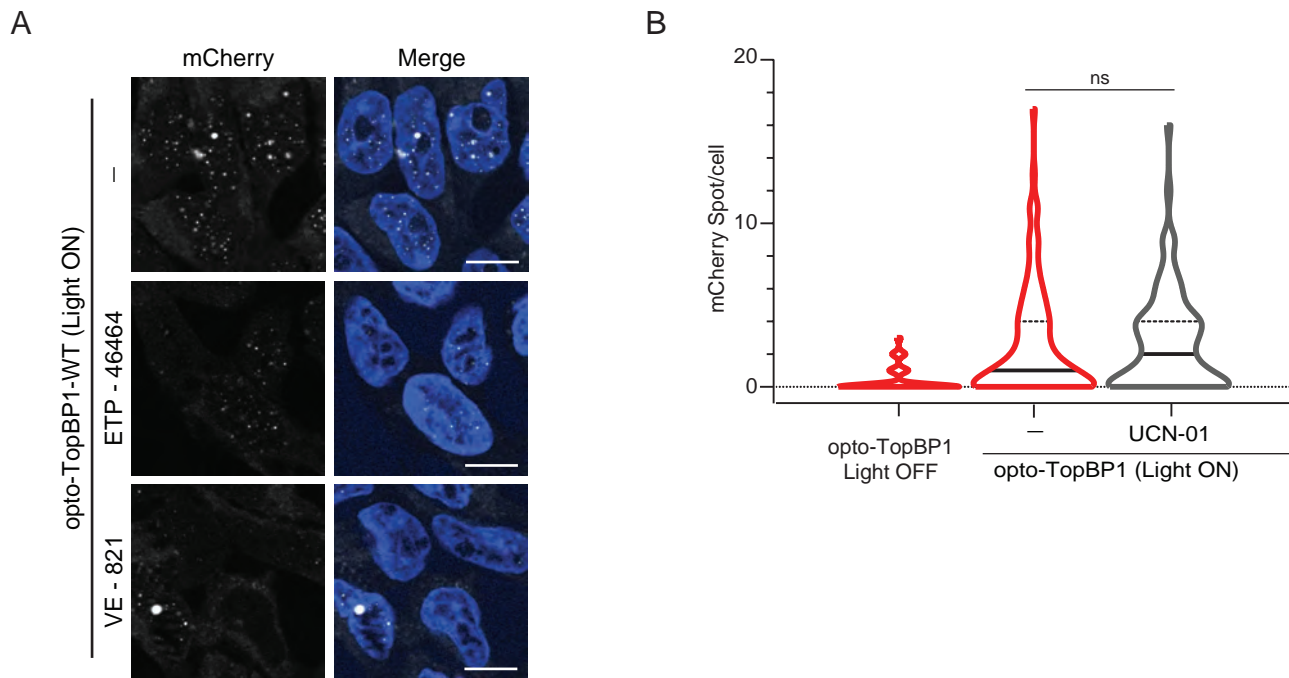
A



B







## SUPPLEMENTAL INFORMATION

**Supplementary video. Related to Figure 2A.** 3D projection of opto-TopBP1 condensates.

**Table S1.** Oligonucleotides used in this study. Related to Key Resources Table and Method Details.

Primers	Sequence
Primer 1 (Fw)	TTGGCGCGCCAtccagaaatgacaaagaaccgt
Primer 2 (Rev)	TTTTCCTTTTGCGGCCGCttagtgtactctaggtcgtttg
Primer 3 (antisense)	GTAGGGTCATCCCTAATGATCTGTTCATTTTGGGAAGGC
Primer 4 (Fw)	GGGGTACCATCGATGCTAGCatggtgtctaaaggcgagga
Primer 5 (Rev)	GGCGCGCCtcagtcacgcatgttcaggt
Primer 6 (Fw)	GGGGTACCACCATGctttctgccagccctca
Primer 7 (Rev)	CTAGCTAGCgtgtactctaggtcgtttgatt
Primer 8 (Fw)	gggCTTAAGgccaccATGaaagacaatactgtgcctctg
Primer 9 (Rev)	cggGGTACCCACGTGcttttcggcagaccgcaga
Primer 10 (Fw)	gggCACGTGtccagaaatgacaaagaaccg
Primer 11 (Rev)	cggGGTACCgtgtactctaggtcgtttgat
Primer 12 (sense)	gagatgagagagaacgctcagaagcagttacag
Primer 13 (sense)	gtcaacacagagcctgcccaaatgaacagatc
Primer 14 (sense)	gtcaacacagagcctgaccaaatgaacagatc
Primer 15 (Fw)	CTAGCGTTTTAACTTAAGATGgctgtgtcttcaacaaaggatg
Primer 16 (Rev)	cctaCATGGTACCatcatgtaaggcttttgaagagg
Primer 17 (Fw)	tacacGGTACCATGaggaaagctctacag
Primer 18 (Rev)	cacatGCTAGCtctaggtcgtttgatttta
Primer 19 (Fw)	AGCTTGGTACCATGAGTCGGCGAAGGAAACATGATG
Primer 20 (Fw)	ccgaaaagCACGTGGGTACCAAGTGCCTGGTCACGGG
Primer 21 (Rev)	atGCTAGCATCGATGGTACCGCCTTCACCCTCACTGTCTTCC
Primer 22 (Rev)	cacatGCTAGCAAGAAATGAAGTGGGAGCTGC

Primer 23 ( Fw )	tacacctggatacaccatcaaaattcctgtccaaggacaaac
Primer 24 (Rev)	CTTTGGTGTTCATAtgagagtagtcgactattacagagccg
Primer 25 ( Fw )	agtcgactactctcaTATGAAACACCAAAGAGAGCGCTGA
Primer 26 (Rev)	agcaatttctgaatcTGACCACATCTGTATATTATCTTTATAAATACTTAAAATCTCTGTTTCT
Primer 27 ( Fw )	ATACAGATGTGGTCAgattcagaaattgctaaacaggctgtct
Primer 28 (Rev)	ttcctgcacgaagtgtccagcagtcctgcaggcttcaaggta

### Supplementary Figure Legends

**Figure S1. Related to Figure 1.** **A)** Immunoblotting of TopBP1. **B)** (Left) Representative fluorescence images of cells expressing opto-RAD9 under control of doxycycline. Light ON: 488nm light. (Right) Immunoblotting of the cells with the indicated antibody. **C)** ETAA1 does not assemble condensates. The construct, representative fluorescence images, and Violin plot representation of quantified condensates are shown, as described in Figure 1.

**Figure S2. Related to Figure 2.** **A)** Representative fluorescence images of cells used for experiments in Figure 2C. DNA stained with Hoechst 33258. Scale bars: 10µm. **B)** (Left) FRAP recordings of two individual eGFP-TopBP1 condensates are reported as examples. Scale bars: 10µm. (Right) Histogram representation of the mean of immobile and mobile fractions per nucleus (13 nuclei, 23 individual spots). **C)** Representative fluorescence images of eGFP-TopBP1 expressing U-2-OS cells treated, when indicated, with 3% of 1,6 Hexanediol. **D-E)** Representative fluorescence images of cells used for experiments in Figure 2D (**D**) and 2E (**E**). DNA stained with Hoechst 33258. Scale bars: 10µm. **F)** Violin plot representing the number of mCherry foci per cell in opto-TopBP1 expressing cells treated with 5mM HU. TopBP1 foci were identified with anti-mCherry antibody after CSK treatment. **A-B-C-D-E-F)** Number of biological replicates = 3.

**Figure S3. Related to Figure 3.** **A)** Representative fluorescence images of cells expressing opto-TopBP1<sup>b6-8</sup> WT before (Light OFF) and after (Light ON) optogenetic activation. DNA stained with Hoechst 33258. Western blotting of the indicated proteins is shown. Violin plot represents the number of mCherry foci per cell. **(B)** Stain-free gel of purified TopBP1<sup>b6-8</sup>-GFP WT and W1145R used for phase separation assays. **(C)** Representative fluorescence microscopy images of TopBP1 condensates assembled *in vitro*. The concentration of TopBP1 is indicated **(D)** Representative fluorescent images of TopBP1 condensates in suspension. DNA stained with Hoechst 33258. Line scan of GFP-Hoechst signals are shown. **A-C-D)** Scale bars: 10 $\mu$ m. Number of biological replicates = 3.

**Figure S4. Related to Figure 4.** Immunofluorescence staining of Flag-BirA\*-TopBP1 WT using anti-Flag antibody. Biotin conjugates were revealed using AlexaFluor streptavidin. DNA stained with Hoechst 33258. Scale bars: 10 $\mu$ m. Number of biological replicates = 3.

**Figure S5. Activation of endogenous ATR in nuclear extracts.** **A)** Nuclear extracts at the indicated protein concentration were incubated in the presence of the ATR inhibitor ETP-46464 (10 $\mu$ M), as indicated. Chk1 activation is revealed by immunoblotting with the indicated antibodies. \* represents unspecific bands. **B)** Immunoblotting of Chk1/pChk1 (Ser345) in reaction mixtures. When indicated nuclear extracts were pre-incubated with ethidium bromide (EtBr). **A-B)** Number of biological replicates = 3.

**Figure S6. Related to Figure 5.** **A)** Immunoblotting analyses of the indicated proteins before and after optogenetic activation of TopBP1 condensates. When indicated, cells were pre-treated with

10 $\mu$ M UCN-01. **B)** Immunoblotting analysis of the indicated biotinylated proteins isolated with streptavidin beads in WT and W1145R opto-TopBP1 expressing cells exposed exposed to 488 nm light, when indicated. **C-D-E)** Immunofluorescence staining with the indicated antibodies of opto-TopBP1 expressing cells activated by light. Line scans are shown. DNA stained with Hoechst 33258. Scale bars: 10 $\mu$ m. Violin plot (**E-right**) representing spot of pChk1 in cells with (dashed white line) or without (solid white line) opto-TopBP1 foci. **F)** Histograms representing the mean of mCherry foci per cell. Cells expressing opto-TopBP1 WT were exposed to 488 nm light, and, when indicated, nuclear soluble proteins were extracted with Cytoskeleton (CSK) buffer. **A-B-C-D-E-F)** Number of biological replicates = 3.

**Figure S7. Related to Figure 6.** **A)** Representative fluorescence images of cells used for optogenetic experiment in Figure 6A. **B)** Violin plot representing the number of mCherry condensates per cell in opto-TopBP1 expressing cells pre-treated for 1h with 10 $\mu$ M UCN-01, when indicated. **C)** Representative fluorescence images of cells used for optogenetic experiment in Figure 6C. **A-B-C)** Number of biological replicates = 3.